WSRA-mappingDWS-20191118 JTECH.docx

Mapping of Directional Wave Spectra in Hurricanes and Other Environments

Ivan PopStefanija

ProSensing Inc., 107 Sunderland Road, Amherst, Massachusetts

C. W. Fairall and Edward J. Walsh

NOAA/Earth System Research Laboratory, Physical Sciences Division, Boulder, Colorado

ABSTRACT

The NOAA Wide Swath Radar Altimeter (WSRA) and its processing are described. The WSRA provides real-time measurements of sea surface significant wave height and directional wave spectra during flights in hurricanes and other environments. The characteristics of near nadir scattering from the sea surface and the resulting distortion of the wave topography measured by the WSRA are discussed, as well as the simulation which generated a matrix to correct the directional wave spectra produced from the WSRA wave topography.

Corresponding author: Ivan PopStefanija, popstefanija@prosensing.com

1. Introduction

Hurricanes draw energy through the air/sea interface, which is characterized by the directional wave spectrum. The present ability to provide targeted measurements of sea surface directional wave spectra is the result of over 40 years of evolution. In the 1970s the Naval Research Laboratory (NRL) developed the 36 GHz Surface Contour Radar (SCR) under the NASA Advanced Applications Flight Experiments (AAFE) program. The SCR produced a topographic map of the sea surface as the aircraft advanced (Kenney et al. 1979; Walsh et al. 1981; Walsh et al. 1985; Walsh et al. 1989). But the volume of the antenna system and the vibration associated with the large oscillating mirror which scanned the beam could only be accommodated by a NASA research aircraft which did not fly in tropical cyclones, where knowledge of underlying ocean waves characteristics would be very valuable to the forecasters and weather modelers.

In the late 1980's the Scanning Radar Altimeter (SRA) mode of the NASA 36 GHz Multimode Airborne Radar Altimeter (Parsons et al. 1994) was developed for installation on NOAA research aircraft that were flying missions into tropical cyclones. The SRA flew for eight hurricane seasons on a NOAA WP-3D aircraft starting in 1998 (Wright et al. 2001; Walsh et al. 2002). The SRA documented the hurricane large scale directional wave spectrum as well as the small-scale roughness and provided useful information for modelers (Moon et al. 2003; Black et al. 2007; Chen et al. 2007; Fan et al. 2009; Hwang and Fan 2017; Hwang and Walsh 2018), but the complex post processing caused a significant delay in its data availability. When the SRA was retired after the 2005 hurricane season, the need for a system that could operate unattended and provide output products in real-time was recognized.

2. Wide Swath Radar Altimeter – instrument description

The NOAA Wide Swath Radar Altimeter (WSRA) is a digital beamforming radar altimeter developed by ProSensing with funding from the NOAA Small Business Innovative Research (SBIR) and Joint Hurricane Testbed (JHT) programs, with additional support from the University of Massachusetts and the Defense Advanced Research Projects Agency (DARPA). The WSRA provides continuous real-time reporting of several data products: (1) significant wave height, (2) directional ocean wave spectra, (3) the wave height, wavelength, and direction of propagation of the primary and secondary wave fields, (4) rainfall rate and (5) sea surface mean square slope (mss). During hurricane flights the data products are transmitted in real-time from the NOAA WP-3D aircraft through a satellite data link to a ground station and on to the National Hurricane Center (NHC) for use by the forecasters for intensity projections and incorporation in hurricane wave models.

The WSRA operates at 16 GHz and its antenna array is comprised of 62 narrow microstrip subarrays that are parallel to the aircraft heading and spaced at half wavelength intervals orthogonal to the aircraft heading. The raw I&Q data are collected for the returns from sequential 150 MHz chirped transmissions on each of the 62 array elements. These Level 0 data, acquired over a 2 to 3 ms interval depending on the aircraft altitude, are coherently combined to produce 80 narrow beams spread over ±30º from the overall antenna boresight. For each of the 80 narrow beams, sixteen return waveforms are averaged incoherently to reduce the Rayleigh fading inherent in the backscattered power so the result well represents the range variation of the radar echo.

Level 1 data, which are the average returned power in each range gate for the selected range interval in each of the 80 narrow beams, are generated at approximately a 10 Hz rate. The

range interval is chosen so that the radar backscatter from the sea surface is present in each of the 80 narrow beams. Level 1 data are high volume and only 300 consecutive sets of 80 return waveforms, acquired over 30 s intervals, are saved at 10-minute intervals on the local onboard WSRA server computer.

Level 2 data contain the centroid range to the sea surface and the integrated backscattered power for each of the 80 narrow beams. The aircraft flight parameters needed for accurate geo-referencing of the WSRA data products are also included in the saved Level 2. At approximately a 10 Hz rate, the ranges from the 64 narrow beams nearest nadir (±23º) are multiplied by the cosines of their various incidence angles to determine the vertical distance to each position across the swath. The aircraft altitude is determined by averaging the 64 heights on each cross-track raster line and then filtering the result along-track to eliminate wave contamination. Subtracting the individual narrow beam vertical distances from the aircraft altitude produces a topographic map of the waves as the aircraft advances.

Figure 1 shows 1620 raster lines of grayscale-coded WSRA wave topography from the 64 beams nearest nadir. The data were acquired in Hurricane Irene on 25 August 2011 while the aircraft flew south in the Bahamas at 2260 m height. The first 800 raster lines make up the left image, top to bottom, and the next 820 lines make up the right image. The wave height variation over the 1620 raster lines was so dramatic that four different gray scales were used to make the details of the evolving wave field apparent.

The northwest tip of Whale Cay (26.714^0N, 77.243^0W) is apparent in Figure 1 at 8.2 km south and 3.4 km east. The incidence plane of the narrow beams is perpendicular to the aircraft heading. A strong wind from the west required the aircraft heading to be about 15^0 west of south to maintain its southern flight track.

3. WSRA measurement geometry

The left image in Figure 2 shows a grayscale-coded map of WSRA sea surface topography in Hurricane Irene on 25 August 2011, generated from the 64 beams nearest nadir for 500 raster lines of WSRA range data acquired as the aircraft flew northwest. The right image is the backscattered power from the same beams after removing the average cross-track and along-track trends. Many details of the wave topography map are in evidence in the backscattered power image. Backscattered power varies with depth into the waves as well as with the tilts of the water surface. In turn, those variations in backscattered power distort the apparent elevation of the water surface determined by the WSRA.

The center (nadir) of the 80 narrow beams has a half-power cross-track width of 1.3º and the off-nadir beawidths widen as 1/cos θ. In the along-track direction the antenna beamwidth is 2.1 degrees, determined as $\lambda\!\!\!^{-}/D$ where $\lambda\!\!\!^{-}$ is the wavelength of the radar signal and D is the 60 cm antenna dimension in the along-track direction.

Figure 3 is drawn in proportion showing one of the WSRA 80 narrow beams, represented by a Gaussian gain variation, boresighted on a flat sea surface from 2400 m at a 23º off-nadir incidence angle. The lines of short dashes extending from the upper left indicate the beam boresight and its half-power limits. The lines of long dashes show how the gain variation across the beam would translate into the range variation of backscattered power indicated along the beam boresight. Even though the half-power range extent of the backscattered power would be more than 28 m for the angle shown, the centroid range computed by the WSRA would produce an accurate range to the surface if the sea surface radar cross section were uniform.

In Figure 4 the geometry is the same as Figure 3, but the three curves near the dashed mean sea level represent sinusoidal ocean waves of 80, 160 and 320 m wavelength with

wavelength to wave height ratios of 30, which is typical for the higher waves in a hurricane. The antenna beam is boresighted at the crest of the waves.

Consider the three dashed radials (boresight and half power limits) in Figure 4. The wave tilt on the nadir side of the crest reduces the incidence angle and increases the backscattered power. The wave tilt on the off-nadir side of the crest increases the incidence angle, reducing the backscattered power. The shortened centroid range from the skewed backscattered power distribution, assigned to the beam boresight angle, will make the wave crest appear higher than it actually is. Even though the slopes of all three sinusoidal ocean waves are identical, a shorter wavelength produces a larger slope variation within the beam and a proportionally greater apparent crest height increase.

For a wave trough at the boresight, the wave tilt on the nadir side would increase the incidence angle, reducing the backscattered power, while the tilt on the off-nadir side would reduce the incidence angle, increasing the backscattered power and skewing the centroid range longer, increasing the apparent depth of the wave trough. Wave tilt modulation increases the apparent height of waves propagating across the swath and the effect is greater for shorter wavelengths.

4. Backscattered power variation with incidence angle

Correcting for the distortions in WSRA measured wave topography requires a model for the variation of radar cross section with incidence angle. The power backscattered from the sea surface generally decreases in an approximately Gaussian fashion within 10° to 15° of nadir and then falls off more slowly at larger incidence angles (Barrick 1968; Barrick 1974; Valenzuela 1978). The variation has been explained by an analytical sea surface slope model using the

theory of the surface as a two-scale compound process, with large-scale inhomogeneities modulating a normally distributed population of smaller scales (Chapron et al. 2000), and by using only Gaussian sea surface slope statistics and accounting for diffraction effects (Voronovich and Zavorotny 2001).

A quadratic expression (Walsh et al. 2008) for the variation of backscattered power *P* with incidence angle,

$$\ln P(S) = -AS^2 + BS^4 \qquad (1)$$

where *S* is the sea surface slope and *A* and *B* are the linear and quadratic coefficients of the square of sea surface slope, well-matched the theoretical computation at 14 GHz (Voronovich and Zavorotny 2001). The circles in Figure 5 are the theoretical computation and the curves are the fitted quadratic equation (1), which agree well out to incidence angles of about 29º, indicated by the vertical line. *A* is related to the sea surface mean square slope (mss) by

$$A = \text{mss}^{-1} - 2 \qquad (2)$$

Figure 6 shows two examples of the variation of backscattered power with off-nadir incidence angle averaged over 500-line segments of WSRA data. The circles show the power falloff on the right side of the swath in 0.75° increment bins and + symbols show the fall-off on the left side. The top abscissa numbers are in degrees. The curves and *A*, *B* values indicate the result of fitting (1) to the power variations on the right (solid) and left (dash) sides of the swath. Time in seconds of day is indicated below the *A*, *B* values. In the general WSRA processing, the power values from the left and right sides of the swath are averaged but they were kept separate in Figure 6 to demonstrate their consistency.

The data in the top plot, corresponding to an mss of 0.023, were acquired in Tropical Storm Karen when the wind speed at the 2552 m altitude was 10 m/s. The data in the bottom

plot, corresponding to an mss of 0.047, were acquired about 200 km north of the eye of Hurricane Irene while the wind speed at the 2449 m aircraft altitude was 37 m/s.

Figure 7 shows all the *B* vs *A* values determined from WSRA data for four flights. The aircraft altitude was always between 2 to 2.6 km except that about half the low wind test flight data were acquired at 1.6 km. The curve in Figure 7 is the power law

$$B = 0.4182\ A^{1.434} \tag{3}$$

that best fit all the 36 GHz NASA SRA data acquired in the Southern Ocean (Walsh et al. 2008) for wind ranging from 2 to 19 m/s and waves ranging from 1 to 9 m wave height. The general variation of the WSRA 16 GHz data follows the power law that best fit the 36 GHz SRA data.

For every 10 s non-overlapping set of 100 raster lines of WSRA wave topography, the automated processing during the flights determines *A* from the average of the power falloff on the left and right sides of the swath within 14^0 of nadir and converts that to an mss value using (2).

5. Numerical simulation of wave topography distortions

A 3-dimensional numerical simulation was developed which projected the measured gain variation for the WSRA narrow beams, broken into 0.025^0 elements in the along-track plane and 0.05^0 elements in the cross-track plane, onto a long-crested sinusoidal ocean wave. The range to the sea surface for each beam sub-element, weighted by its gain and the radar cross section determined from the specified mss, (2), (3), (1) and the local incidence angle, produced the range variation of backscattered power whose centroid, ascribed to the beam boresight, determined the apparent surface elevation.

Figure 8 shows the wave profiles on the right side of the WSRA swath which were generated by the simulation for an aircraft altitude of 2.5 km and long-crested sinusoidal waves propagating across the swath. The greatest variations in apparent wave height occurred for the lowest mss value, 0.02. For the 320 m wavelength the apparent wave height increased by about a factor of 2.5 toward the swath edge. For the 160 m wavelength the nadir wave height was noticeably reduced and then the wave height increased by about a factor of 5.5 by the edge of the swath, almost reaching the apparent height of the 320 m wavelength. The 80 m wavelength apparent wave height was greatly reduced at nadir, significantly increased toward the swath edge, and significantly distorted in profile.

If the wave propagation direction had been parallel to the aircraft flight direction, there would have been no tilt modulation of the incidence angle by the long crests of the waves extending in the plane of incidence of the WSRA beams.

A correction matrix was generated for seventeen different wavelengths (37 m to 800 m) propagating in seven different directions (0^0 through 90^0) relative to the plane of incidence of the narrow beams for seven different values of mss (0.08, 0.065, 0.05, 0.035, 0.027, 0.02, 0.0125).

Twenty-seven narrow-beam boresights were used (0^0 to 26^0 off-nadir) to determine how the apparent wave height would vary across the WSRA swath. For each beam boresight, the computation was repeated 36 times with the phase of the ocean wave at the boresight incrementing from 0^0 to 350^0 to establish a measured wave profile and determine the apparent wave height for the off-nadir angle of the beam boresight.

In general, the apparent wave height near nadir will be less than the actual wave height and the apparent wave height near the swath edges will be greater. The simulation computes the overall average of the variance for the apparent wave height variation over the entire swath.

There is less power returned to the radar as the off-nadir incidence angle increases because of reduced antenna gain and the falloff of radar cross section. If it rains, the attenuation initially reduces the WSRA signal below a useable level at the edges of the swath and then progressively narrows the swath as the rain rate increases. The effective incidence angle width of the swath is taken into account in determining the wave spectral variance correction.

When correcting spectral data acquired at heights other than 2500 m, the wavelength entry into the correction matrix is simply scaled. A 160 m wavelength observed from 1.25 km height would look like a 320 m wavelength observed from 2.5 km height.

6. Directional wave spectra

During the flights the WSRA data are collected continuously without gaps, and the measured sea surface elevations are stored in Level 2 (L2) files containing 2700 raster lines, where each line contains an across track swath of 80 elevations. A segment of wave topography (segment size: 300 lines along track by 64 near-nadir elevations across-track) is interpolated onto a square grid of 256 by 256 points spaced at 10-m intervals, centered on the 300 lines and oriented in the aircraft flight direction.

At an aircraft ground speed of about 85 m/s, 300 across-track raster lines of elevations are contained within the 256 by 256-point square grid. Figure 9 illustrates the large variation of the aircraft ground speed during the flight in Hurricane Irene on 25 August 2011. The aircraft made five passes through the eye. On the four intervening legs, where it was repositioning for the next eye pass, the strong tailwind increased the ground speed to about 170 m/s.

Figure 9 indicates a ground speed of 128 m/s (horizontal dashed line) is a good approximation for the aircraft ground speed during the eye passes. At that speed, only the center

200 of the 300 WSRA raster lines would be contained within the 256 by 256-point square grid used to produce the individual spectra.

A two-dimensional FFT transforms the gridded elevations into an individual directional wave spectrum. Twenty-five interpolated square grids of elevations are produced from each 2700-line L2 file while incrementing the starting line number by 100 for each individual spectrum. The WSRA Level 3 (L3) spectra are averages of five consecutive individual spectra so the 2700 raster lines of elevations in each L2 file produces five L3 average spectra. Figure 10 shows the data processing timing diagram for calculating L3 output spectra from raster lines of sea surface elevations stored in the L2 file. The overlap in consecutive L3 output spectra is 10% for ground speed of 128 m/s, while at low (85 m/s) and high (160 m/s) values for ground speed the overlap would be about 20% and 7% respectively.

Level 3 spectra, along with other environmental characteristics derived from the WSRA data such as sea surface mean square slope (mss) and rain rate, as well as the aircraft flight parameters, are transmitted in data packets every 4.5 minutes via a satellite data link to a ground station. The WSRA operates unattended during the flights and the data acquisition and processing is independent of the environment, whether it is a hurricane in the Atlantic Ocean or a uniform wave field in the Pacific Ocean. For a hurricane, the only human input in the ground station processing is to ensure that the latest hurricane position is included.

Level 4 (L4) spectra, generated by the ground station processing, are the final data product, resulting from deleting the artifact lobes (described in the Appendix) and Doppler-correcting and variance-correcting the L3 spectra.

The L4 output spectra have 65 by 65 spectral values oriented in a north and east reference frame and centered on zero wavenumber. The spacing of the points in k-space is 0.002454

radian/m. The east wavenumber values of the columns vary from -0.07854 (left) to 0.07854 (right). The north wavenumber values of the rows vary from -0.07854 (line 1) to 0.07854 (line 65). The shortest wavelength along the coordinate axes is 80 m (0.07854 radian/m wavenumber) and 57 m (0.01111 radian/m wavenumber) at the spectrum corners. The spectrum variance numbers are in m^2. To obtain spectral densities in $m^4/radian^2$, divide the variance values by $6.024*10^{-6}$ $radian^2/m^2$, the area covered by each spectral point. The wave numbers vectors, representing x and y coordinates for each point in the WSRA directional spectra are stored in L4 files as variables: "***wavenumber_east***" for x-axis and "***wavenumber_north***" for y-axis.

The WSRA processing calculates significant wave height (SWH) from the L4 directional wave spectra, now fully corrected, as four times the square root of the spectra's zeroth-order moment. The WSRA calculates SWH at 50 second intervals. At an altitude of 2500 m and a ground speed of 128 m/s, the WSRA SWH estimate represents approximately 14 km^2 area of the ocean.

7. Validation analysis of WSRA directional wave spectra

A flight on 9 February 2015 during the CalWater 2015 experiment (Ralph et al. 2016) provided an excellent opportunity to exhibit the scattering distortions of the wave topography measured by the WSRA and the ability of the automated processing to correct the output directional wave spectra. Figure 11 shows four areas that were about 300 km off the California coast. Each area contained 1300 raster lines of WSRA data which will be analyzed in detail.

The environmental conditions were such that the wave field could be assumed to vary slowly spatially. Figure 12 shows 1700 raster lines of WSRA wave topography collected while

the aircraft was flying northwest and the wind at the 2380 m aircraft height was blowing towards the east at 9.8 ±0.4 m/s. Segment A in Figure 11 included 1300 of those 1700 raster lines.

It was an unusual situation in that there were two wave systems of comparable wavelength and wave height propagating at right angles to each other. Figure 13 shows three L4 spectra generated from the wave topography of Figure 12. The upper right corner of each Figure 13 spectrum contains the total $H_{1/3}$ and the spectrum peak variance in m^2. There are nine solid contours uniformly spaced from 0.1 to 0.9 of the spectral peak with a wide 0.5 contour and a dashed contour at the 0.05 level. The spectrum headers contain wave height, wavelength and direction of propagation of the primary and secondary wave fields. A dashed radial separates the primary and secondary wave fields. The upper left corner contains the seconds of the day for the center of the data span used to generate the spectrum. The lower left corner contains the aircraft height and year, month, day, hour, minute, second of the start of corresponding L2 file. Latitude and longitude are in the lower right corner. The blue radial is wind speed (m/s)*0.001 in the downwind direction at the aircraft altitude. The black radial is the aircraft track and the red radial is aircraft heading.

The Figure 13 spectra provide a sense of the variability existing in the spectra of a nominally uniform wave field. The secondary wave field, a southeast propagating swell, was probably an old system and its characteristics showed little variation in wave height (3.4, 3.4, 3.3 m) and propagation direction (143^0, 143^0, 140^0) with a peak wavelength of 201 ±12 m. Still, its peak spectral variance varied by a factor of almost 2. The northeast propagating wave system was broader and showed more variability with the propagation direction varing by 27^0 and the peak wavelength varying by 68 m.

In the first two sets of 1300 raster lines of WSRA wave topography shown in Figure 11, the aircraft flight direction was initially aligned with one of the systems when it was flying northwest (A) and then it turned towards the northeast (B) and was aligned with the other system.

To demonstrate the effectiveness of the variance correction simulation, directional wave spectra were generated from each set of 1300 raster lines of WSRA topography from the areas identified in Figure 11. The four spectra shown in Figure 14 were each an average of 11 individual spectra instead of the standard 5-spectra averages of Figure 13. This was a compromise between reducing the inherent variablilty in the wave spectra and keeping the result localized.

The three spectra in Figure 13 were generated from raster lines 1001-2700 in the L2 file starting at 21:30:48 UTC. Spectrum A in Figure 14 was generated from raster lines 1301-2600 of that same L2 file. Shortly after the next L2 file began at 21:34:57 UTC, the aircraft turned toward the northeast. Spectrum B was generated from lines 601-1900 when the aircraft was flying straight and level again.

Spectrum C was generated from raster lines 1301-2600 of the L2 file that began at 21:43:14 UTC. When the next L2 file began at 21:47:22 the aircraft was still flying northeast. After it turned toward the southeast, raster lines 1101-2400 were used to generate spectrum D.

In the standard automated processing, an area surrounding the spectral peak is zeroed out and the peak of what remains determined. If a saddle point exists between the spectral peak and the secondary peak, the azimuth of the minimum value determines the partition boundary between the primary and secondary wave fields. For the spectra of Figure 14 the partition

boundary was fixed at 105^0 for consistency because the automated processing placed the partition boundary for spectrum D at 74^0.

For the southeast swell, the average of the header information at position AB was 3.5 m wave height propagating towards 144.5^0. At position CD it was 3.45 m wave height propagating towards 142^0, nearly identical.

For the northeast wave system, the header information averaged 3.9 m wave height propagating towards 73.5^0 at AB and 3.55 m wave height propagating towards 43^0 at CD. The northeast wave system evolved more spatially than the southeast system and that is apparent in the wave spectral contours. The northeast wave system was bimodal in the AB area with a 200-m wavelength component propagating towards 73^0 and a 250-m wavelength component propagating towards 50^0. At position CD the northeast wave field was more narrow, oscillating about 250 m wavelength and 45^0 propagation direction.

The variance-corrected wave spectra of Figure 14 document a complex but slowly evolving wave field. Figure 15 shows the same four spectra before the variance correction. At position AB the header information is nearly identical before and after the variance correction for the wave system which happened to be aligned with the aircraft flight direction, the southeast swell at position A, 3.4m, 207m, 143^0 (before, Fig. 15) vs 3.3m, 207m, 143^0 (after, Fig. 14), and the northeast wave system at position B, 4.3m, 194m, 74^0 (before, Fig. 15) vs 4.1m, 194m, 74^0 (after, Figure 14).

The big distortion in wave topography results from backscattered power modulation by the surface tilts of waves propagating perpendicular to the aircraft heading. At position A the northeast wave system height was 59% higher before the variance correction (5.9 vs 3.7 m). At position B the southeast swell was 57% higher before the correction (5.8 vs 3.7 m). The peak

wavelengths were also shorter before the correction (198 vs 206 m at A and 218 vs 225 m at B) because the wave topography distortion is greater for shorter wavelengths.

The Figure 15 spectral contours dramatically document the wave tilt modulation distortion effect without considering any of the numbers. Without the variance correction, the northeast wave system was dominant at location A. But just after turning the corner, the southeast swell was dominant at location B. The southeast swell maintained its dominance while the aircraft traveled 70 km up to location C, but when the aircraft turned toward the southeast it immediately lost its dominance at location D.

The filled circles in Figure 16 show the cross-track variation of the apparent wave height, computed as four times the standard deviation of the elevations at each of the 64 cross-track positions of the wave topography. They were generated from segments of 300 consecutive raster lines approximately centered on the raster line segments used to generate the spectra of Figures 14 and 15. The open circles indicate the number of valid elevations at each cross-track position.

Since there is only spatial filtering by the antenna footprint at nadir, the minimum wave height values at all four locations (A, B, C, D) are about 3.3 m. The wave tilt backscattered power modulation distorting the wave topography increases as the mss decreases. The dramatic wave height increases to about 20 m at the swath edges for locations A, B and C result from the low mss, 0.027. The wave height increase was less at position D because the aircraft heading was not perpendicular to a wave system propagation direction as it was in the other three cases.

The number of valid elevations tends to decrease very rapidly after it has declined to 80%. The automated processing generating each of the 25 individual spectra from the L2 files zeros out all elevations at cross-track positions which have fewer than 240 valid elevations in the 300-line segment, indicated by the top horizontal dashed lines in Figure 14.

The automated processing also zeros out elevations at cross-track positions where the wave height exceeds five times the nadir wave height. That limit is indicated by the middle dashed horizontal line. To keep random fluctuations from complicating the procedure, the cross-track variation of the wave height values is filtered by a 5-point moving average, indicated by the line through the filled circles.

The middle dashed vertical line and the lower dashed horizontal line indicate the cross-track position of the wave height minimum and its value. The left and right vertical dashed lines indicate the more restrictive of the two editing criteria. The 80% valid elevations is generally the more restrictive criterion and that is the situation at locations A and D. But because of the low mss and the orientation of the wave systems, the other criterion was more restrictive at location B and at the left side of the swath at location C.

FFTs represent topography as a linear superposition of long-crested sinusoids. The simulation generating the wave spectrum variance correction matrix computed the distorting effect of power backscattered from the surface areas of individual long-crested sinusoidal waves that do not exist in the real world. In the real world, the orientation of the sea surface area backscattering the power is a composite result of all the waves present. It is not obvious that the backscatter from the actual sea surface would be the same as a superposition of the backscatter from the individual long-crested sinusoidal waves. In a hurricane the wave field generally varies rapidly spatially, making it difficult to assess the performance of the correction. However, the complex but slowly varying wave field observed during Calwater 2015 (Figures 11 through 16) demonstrated that the spectral variance correction matrix is effective in correcting even the large topographic distortions resulting from a low mss environment.

8. Hurricane Irene wave field map

Figures 17 and 18 demonstrate some of the detail information on the wave field that the WSRA provides in real-time. In geographic coordinates, Figure 17 shows vector maps of the WSRA primary and secondary wave fields observed during the 25 August 2011 flight into Hurricane Irene. The radials extend from the observation locations in the wave propagation direction a distance proportional to the wavelength of the primary (left side) and secondary (right side) wave fields. The width of the radials is proportional to wave height and they are color coded in four wave height intervals.

To reduce the amount of overlap of the radials, subsequent locations plotted had to be at least 10 km from the previous location. At the typical 128 m/s ground speed of the aircraft there is about 6 km between adjacent L4 output directional wave spectra, so only about every other L4 spectral location is displayed in Figures 17 and 18. Data from locations where the wave topography was contaminated by land were excluded.

The complex geographic environment of the Hurricane Irene flight significantly affected the wave height spatial variation. The automated artifact lobe deletion process does not consider the presence of land or shallow water, but it still produced excellent results in general.

Irene was tracking a little west of north at about 4.8 m/s and moved about 84 km during the 4.7 hours between the first and fifth eye penetrations on the August 25 flight. Figure 18 presents the WSRA data in a storm-relative reference frame.

The primary and secondary wave fields are automatically assigned on a basis of wave height. In regions where the wave height of two wave systems is approximately the same, the assignment can appear to switch back and forth randomly.

North of the eye the wave field was less affected by the islands and shallow water and showed the typical hurricane complexity. The wind and primary wave directions were nearly aligned in the right front quadrant of Figure 18 (100 km N, 100 km E). In the left front quadrant (100 km N, -160 km E) there was a secondary wave field nearly aligned with the local wind, but the primary waves propagated almost orthogonal to the wind. The relative variation of the wind and wave directions could impact things like flow separation and energy transfer at the surface.

9. WSRA output data products

The WSRA real-time processing produces the following data products: (1) significant wave height (SWH), (2) directional ocean wave spectra, (3) the wave height, wavelength, and direction of propagation of the primary and secondary wave fields, (4) rainfall rate and (5) sea surface mean square slope (mss).

The WSRA significant wave height is reported live to the NOAA National Hurricane Center in Miami using a simple ASCII message containing time, latitude, longitude, and SWH. The sampling interval of the reported SWH is 50 seconds, while spatial resolution is approximately 6.4 km in along track direction and 2 km in across track direction

The WSRA data products, processed to Level-4, are stored and archived for further post-flight analysis. The WSRA L4 files are formatted in NetCDF (network Common Data Format), insuring compatibility with a large number of visualization and data analysis software applications.

Definitions of all variables present in the WSRA Level-4 data file (in the netCDF format) are shown in Table 1. Variable names used in the netCDF file are highlighted in **bold**. The output wave spectra are contained in **directional_wave_spectrum**. Because the automated

artifact lobe deletion process might occasionally delete the wrong lobe, a Level-3 wave spectrum file is also included (**directional_wave_spectrum_180**) in which all spectral components (real and artifact) have been Doppler and variance corrected (Figures A1 and A2). This allows an investigator to evaluate WSRA directional ocean wave spectra without being subject to the artifact lobe deletion algorithm.

10. Conclusions

The WSRA can provide real-time targeted measurements of wave fields in hurricanes and other environments. The 180° ambiguity present when wave topography maps are transformed into directional wave spectra can generally be eliminated automatically in the vicinity of a hurricane by using a model to simulate the integrated forcing effect of the wind field. Variations in the backscattered power caused by the tilts of the sea surface waves being measured can distort the apparent wave topography, but the spectral variance correction matrix developed is effective in correcting for even the large topographic distortions occurring in a low mss environment.

The NASA SRA, the forerunner of the NOAA WSRA, measured the storm surge in Hurricane Bonnie (Wright et al. 2009). The WSRA could also provide targeted measurements of storm surge if the absolute height of the aircraft was determined by GPS.

Acknowledgment. The NOAA Aircraft Operations Center installs and operates the WSRA.

APPENDIX

Artifact spectral lobe deletion

Two wave systems are apparent in the Figure 2 wave topography image. A long wave system was nearly aligned with the aircraft flight track and a shorter wave system propagated orthogonal to the track. It is not possible to tell from the topography if the long waves were traveling northwest or southeast or if the short waves were traveling southwest or northeast. The Level 3 ocean wave spectra are generated using the two-dimensional FFT which deposits half the energy of each wave system in a real lobe corresponding to the wave propagation direction and half in an identical artifact lobe propagating in the opposite direction.

The Level 3 average wave spectra are truncated to 65 by 65-point arrays centered on zero wavenumber with 0.00245 rad/m resolution and contained within ±0.08 rad/m in k-space. Figure A1 shows two WSRA directional wave spectra from the Calwater 2015 flight on 9 February 2015 which have been Doppler- and variance-corrected but have not had the artifact lobes deleted. The bottom spectrum is from the middle of area A in Figure 11 and the top spectrum is from the middle of area B. The red, green and blue dots are in identical, symmetrical positions in both spectra. The real spectral lobes are in the right half plane and the red, green and blue dots were positioned to approximate the average of the real spectral peaks in the two spectra.

Multiple measurements of the same wave field will always exhibit minor variations in the details (Figure 13) and the variations would be expected to be larger when the physical locations are different. But if the two spectra of Figure A1 were superimposed, the real lobes in the right half plane would overlap quite well. The artifact lobes in the left half plane would appear mismatched.

In the time it takes to acquire the wave topography data to produce a directional wave spectrum, waves propagating in the aircraft flight direction will move away from the aircraft and

appear to have a longer wavelength while waves propagating in the opposite direction will appear shorter in the wave topography. Waves propagating in other directions will generally appear to have both different wavelengths and directions of propagation.

The real and artifact lobes in the encounter directional wave spectrum (L3) generated by the two-dimensional FFT applied to the WSRA wave topography are perfectly symmetrical. The Doppler correction applied to an encounter spectrum assumes all spectral components are real. A spectral lobe propagating in the aircraft flight direction would have too long a wavelength in the encounter spectrum and would be shifted to higher wavenumbers. A spectral lobe propagating in the opposite direction would have too short a wavelength in the encounter spectrum and would be shifted to lower wavenumbers.

In general, the first order correction shifts all wave components in the aircraft flight direction. The real lobes are shifted into their proper positions and the artifact lobes are shifted in the wrong direction, out of their symmetrical positions. In Figure A1 it is apparent that the artifact lobes are shifted in the aircraft flight direction.

Figure A2 shows two WSRA directional wave spectra from Hurricane Irene which have been Doppler- and variance-corrected but have not had the artifact lobes deleted. The spectra are from passes through the eye flying south (top) and northwest (bottom). The two data sets were separated by 73 minutes and Hurricane Irene had traveled 18 km in that time. But if the characteristics of the storm did not change, the storm-relative wave field could be assumed unchanged.

Since the wave spectra were unimodal in this case, the automated header information identifying two wave components was retained in Figure A2. The northwest wave component was the real lobe and had the same propagation direction (-63^0) in both spectra. The peak

wavelengths agreed within 18 m and the wave heights differed by 0.4 m. The southeast wave component was the artifact lobe. In the two spectra their propagation directions differed by 17^0. The wave heights differed by 1.3 m and the wavelengths differed by 195 m. As in Figure A1, the artifact lobes are shifted out of their symmetrical positions in the aircraft flight direction.

Figures A1 and A2 demonstrate that it is possible to identify the real and artifact spectral lobes without *a priori* information whenever there are wave spectra from significantly different flight tracks in the same area.

If the aircraft were changing the flight direction 90^0 to the right as it did in Figure A1, it would be optimum to accomplish that by turning 270^0 towards the left so the two flight tracks would cross. Due to time constraints, that is generally not done, resulting in a significant separation of the locations where the aircraft is flying straight and level before and after a turn. In the case of Figure A1 it was 19 km. The wave field for Figure A1 was varying slowly spatially. In a hurricane flight, the wave field generally changes rapidly spatially and sometimes both the real and artifact lobes are mismatched when the aircraft changes flight direction. But even in that instance, correlating the directions in which the lobes are mismatched with the flight directions can generally sort things out.

The automated processing for hurricane flights does not rely on the technique just described. Instead, it uses a hurricane wind model (Willoughby et al. 2006; Zhang and Uhlhorn 2012) to generate a wind forcing pattern to predict the propagation direction for waves of various lengths. In 10 km steps outward from the WSRA observation point, the square of the model wind component directed toward the observation point is integrated on every 5^0 azimuth to generate an effective wind forcing pattern. For each 10 km step outward from the observation point, an earlier position of the hurricane is used, determined by the transit time to the observation point at

the group velocity of the ocean wavelength under consideration. The centroid of the wind forcing pattern specifies the direction that waves of that wavelength are predicted to be propagating.

Wind forcing patterns are computed for eight different wavelengths: 366, 256, 197, 160, 135, 116, 102 and 91 m. The distances from the observation point that the wind is integrated over vary from 559 km (13 hours) for the longest wavelength to 129 km (6 hours) for the shortest. The dots in Figure A3 indicate the 65 by 65 positions in the WSRA directional wave spectra. The alternating red and green colors identify the eight regions of the spectrum that the predicted wave propagation directions are applied to.

The elimination of the artifact lobes is done in an iterative fashion. The peak of the L3 directional wave spectrum is determined. The two peak locations (real and artifact) are Doppler-corrected, which will generally change both their wavelengths and propagation directions. The peak whose propagation direction is nearest to the propagation direction assigned to the closest of the eight wavelengths (Figure A3) is deemed the real lobe. It and the surrounding non-zero values within the square in Figure A4 are transferred to an output array. Non-zero values between the square and the octagon are also transferred to the output array if they continue to decrease.

All the values transferred to the output array and the corresponding artifact values in the L3 spectrum are zeroed out and the peak of what remains is determined. The procedure is repeated until the peak of what remains is below 0.5% of the original L3 spectrum peak.

For a non-hurricane flight, the orientations of the eight predicted wave propagation directions are simply specified. It allows for the possibility that a long wavelength swell could be propagating eastward while a short wavelength wind-driven system propagated westward. For the 9 February 2015 flight off the California coast, the wave systems were propagating in the

right half plane and the propagation directions for the eight wavelengths were all set to 90^0. In a more complex situation, the wave propagation direction specifications could vary temporally and/or spatially.

REFERENCES

Barrick, D. E., 1968: Rough surface scattering based on the specular point theory. *IEEE Trans. Antennas Propag.*, **AP-16**, 449-454.

Barrick, D. E., 1974: Wind dependence of quasi-specular microwave sea scatter. *IEEE Trans. Antennas Propag.*, **AP-22**, 135-136.

Black, P. G., E. A. D'Asaro, T. B. Sanford, W. M. Drennan, J. A. Zhang, J. R. French, P. P. Niiler, E. J. Terrill, E. J. Walsh, 2007: Air-Sea Exchange in Hurricanes: Synthesis of Observations from the Coupled Boundary Layer Air-Sea Transfer Experiment. *Bull. Am. Met. Soc.*, **88**, 357-374.

Chapron, B., V. Kerbaol, D. Vandemark, and T. Elfouhaily, 2000: Importance of peakedness in sea surface slope measurements and applications. *J. Geophys. Res.*, **105**, 17 195–17 202.

Chen, S. S., J. F. Price, W. Zhao, M. A. Donelan, E. J. Walsh, 2007: The CBLAST-Hurricane Program and the Next-Generation Fully Coupled Atmosphere-Wave-Ocean Models for Hurricane Research and Prediction. *Bull. Am. Met. Soc*., **88**, 311-317.

Fan, Y., I. Ginis, T. Hara, C. W. Wright and E. J. Walsh, 2009: Numerical simulations and observations of surface wave fields under an extreme tropical cyclone, *J. Phys. Oceanogr.*, **39**, 2097–2116.

Hwang, P. A., and Y. Fan, 2017: Effective fetch and duration of tropical cyclone wind fields estimated from simultaneous wind and wave measurements: Surface wave and air-sea exchange computation. *J. Phys. Oceanogr*., **47**, 447-470, doi: 10.1175/JPO-D-16-0180.1.

Hwang, P. A., and E. J. Walsh, 2018: Propagation directions of ocean surface waves inside tropical cyclones. J. Phys. Oceanogr., **48**, 1495-1511, doi: 10.1175/JPO-D-18-0015.1.6.

Kenney, J., E. Uliana, E. Walsh, 1979: The Surface Contour Radar, a unique remote sensing instrument. *IEEE Transactions Microwave Theory and Techniques*, **MTT-27**, 12, 1080-1092.

Moon, Il-Ju, Isaac Ginis, Tetsu Hara, H. L. Tolman, C. W. Wright and E. J. Walsh, 2003: Numerical simulation of sea surface directional wave spectra under hurricane wind forcing. *J. Phys. Oceanogr.*, **33**, 1680-1706.

Parsons, C. L., E. J. Walsh, and D. C. Vandemark, 1994: Topographic mapping using a multibeam radar altimeter. *IEEE Trans. Geosci. Remote Sens.*, **32**, 1170-1178.

Ralph, F. M., K. A. Prather. D. Cayan, J. R. Spackman, P. DeMott, M. Dettinger, C. Fairall, R. Leung, D. Rosenfeld, S. Rutledge, D. Waliser, A. B. White, J. Cordeira, A. Martin, J. Helly, J. Intrieri, 2016: CalWater Field Studies Designed to Quantify the Roles of Atmospheric Rivers and Aerosols in Modulating U.S. West Coast Precipitation in a Changing Climate. *Bull. Amer. Meteor. Soc.*, **97**, 1209-1228**.**

Valenzuela, G. R., 1978: Theories for the interaction of electromagnetic and oceanic waves - a review. *Bound.-Layer Meteor.*, **13**, 61–85.

Voronovich, A. G., and V. U. Zavorotny, 2001: Theoretical model for scattering of radar signals in Ku- and C-bands from a rough sea surface with breaking waves. *Waves in Random Media*, **11**, 247–269.

Walsh, E. J., D. Hancock, D. Hines, J. Kenney, 1981: Surface Contour Radar remote sensing of wave spectra, *Proceedings of Conference on Directional Wave Spectra Applications '81 Symposium*, ed. R. Wiegel, 281-298.

Walsh, E. J., D. Hancock, D. Hines, R. Swift, J. Scott, 1985: Directional wave spectra measured with the Surface Contour Radar. *Journal of Physical Oceanography*, **15**, 5, 566-592.

Walsh, E. J., D. Hancock, D. Hines, R. Swift, J. Scott, 1989: An observation of the directional wave spectrum evolution from shoreline to fully developed. *J. Physical Oceanography*, **19**, 5, 670-690, 1989.

Walsh, E. J., C. W. Wright, D. Vandemark, W. B. Krabill, A. Garcia, S. H. Houston, S. T. Murillo, M. D. Powell, P. G. Black, and F. D. Marks, 2002: Hurricane directional wave spectrum spatial variation at landfall. *J. Phys. Oceanogr*., **32**, 1667-1684.

Walsh, E. J., M. L. Banner, C. W. Wright, D. C. Vandemark, B. Chapron, J. Jensen, and S. Lee, 2008: The Southern Ocean Waves Experiment, Part III. Sea surface slope statistics and near nadir remote sensing. *J. Phys. Oceanogr*., **38**, 670-685.

Willoughby, H. E., R. W. R. Darling, and M. E. Rahn, 2006: Parametric representation of the primary hurricane vortex. Part II: A new family of sectionally continuous profiles, *Mon. Wea. Rev.*, **134**, 1102-1120.

Wright, C. W., E. J. Walsh, D. Vandemark, W. B. Krabill, A. Garcia, S. H. Houston, M. D. Powell, P. G. Black, and F. D. Marks, 2001: Hurricane directional wave spectrum spatial variation in the open ocean. *J. Phys. Oceanogr*., **31**, 2472-2488.

Wright, C. W., E. J. Walsh, W. B. Krabill, W. A. Shaffer, S. R. Baig, M. Peng, L. J. Pietrafesa, A. W. Garica, F. D. Marks Jr., P. G. Black, J. Sonntag, B. D. Beckley, 2009: Measuring

storm surge with an airborne Wide-Swath Radar Altimeter. *J. Atmospheric Oceanic Tech*., **26**, 2200-2215.

Zhang, J. A., and E. W. Uhlhorn, 2012: Hurricane sea surface inflow angle and an observation-based parametric model. *Mon. Wea. Rev.*, **140**, 3587-3605.

Table 1. Description of Level-4 netCDF file variables

• **directional_wave_spectrum** contains all (Level 4) directional ocean wave spectra from the flight. The artifact spectral lobes have been deleted in the Level-4 spectra and the real spectral lobes have been Doppler-corrected for the motion of the waves during the data acquisition interval and variance-corrected for distortions in the wave topography measured by the WSRA. Variance values are in m^2.

• **directional_wave_spectrum_180** contains (Level-3) directional wave spectra containing both real and artifact spectral lobes which have been Doppler-corrected and variance-corrected.

• **dominant_to_secondary_partition_angle** indicates the North relative angle as boundary between the dominant and secondary wave fields if two have been identified.

• **dominant_wave_direction** is the propagation direction of the dominant wave field in degrees.

• **dominant_wave_height** is the significant wave height of the ocean dominant wave field in meters.

• **dominant_wave_wavelength** is the peak wavelength of the ocean dominant wave field in meters.

• **hurricane_eye_distance_east** is the distance east of the hurricane eye in km.

• **hurricane_eye_distance_north** is the distance north of the hurricane eye in km.

• **latitude** in degrees

• **longitude** in degrees

• **peak_spectral_variance** is the peak spectral variance in m^2 of the Level 4 directional ocean wave spectra.

• **platform_course** is the North-relative aircraft track angle received from aircraft IWG1 in degrees.

• **platform_orientation** is North-relative aircraft heading received from aircraft IWG1 in degrees.

• **platform_radar_altitude** is the aircraft altitude in meters determined by the WSRA.

• **platform_speed_wrt_ground** is the aircraft ground speed received from aircraft IWG1 in m/s.

• **rainfall_rate** - five independent values of rain rate (mm/hr) determined at -20, -10, 0, 10, 20 s displacements relative to the observation time.

• **rainfall_rate_median -** median value of the 5 values in rainfall_rate.

• **sea_surface_mean_square_slope** - five independent values of mean square slope (mss) determined at -20, -10, 0, 10, 20 s displacements relative to the observation time.

• **sea_surface_mean_square_slope_median -** median value of the 5 values in sea_surface_mean_square_slope

• **sea_surface_wave_significant_height** (SWH) in meters.

• **secondary_wave_direction** is the propagation direction of the secondary ocean wave field in degrees, if one exists.

• **secondary_wave_height** is the significant wave height of the secondary ocean wave field in meters, if one exists.

• **secondary_wavelength** is the peak wavelength of the secondary ocean wave field in meters, if one exists.

• **time** is the time of the observation in seconds since the start of the observation specified in the file's global attribute "time_coverage_start"

• **wsra_computed_roll** is average WSRA computed roll determined at -20, -10, 0, 10, 20 s displacements relative to the observation time.

• **trajectory** is a unique identifier for observation instant.

• **wavenumber_east** is the set of 65 spectral wavenumber values along the east axis.

• **wavenumber_north** is the set of 65 spectral wavenumber values along the north axis.

• **wind_direction** – upwind direction at the aircraft altitude in degrees.

• **wind_speed** at the aircraft altitude in m/s.

• **wave_direction_predicted** - predicted direction of propagation for eight wavelengths (366, 256, 197, 160, 135, 116, 102, 91 m) computed to aid in deleting artifact lobes.

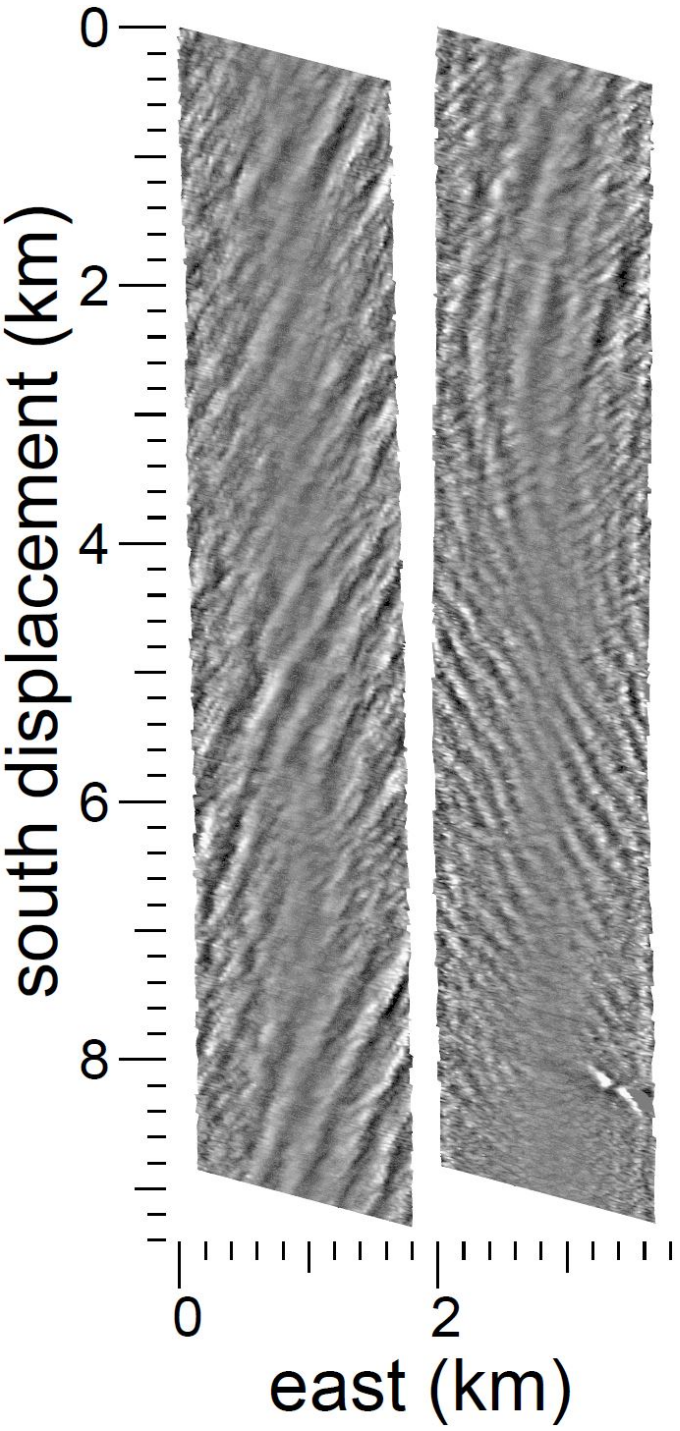

FIG. 1. WSRA grayscale-coded wave topography. The first 800 raster lines are in the left image with a grayscale spanning 5 m (white) to -5 m (black) for the top 400 lines and ±4 m grayscale for the bottom 400. The next 820 raster lines are in the right image with the top 410 lines using a ±3 m grayscale and the bottom 410 lines using ±2 m.

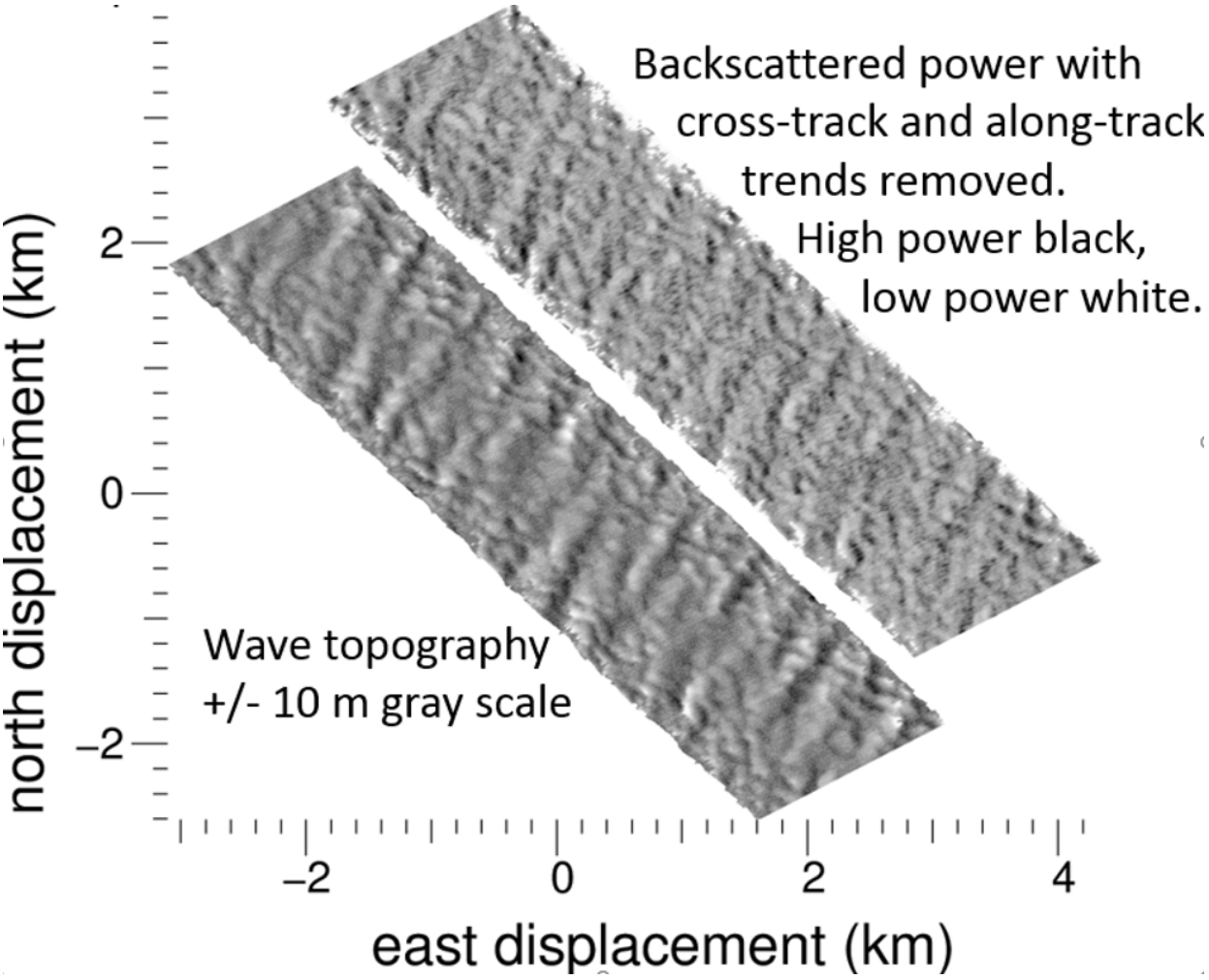

FIG. 2. The WSRA wave topography image goes from -10 m (black) to 10 m (white). The sense of the backscattered power image is reversed, with lowest power being white and highest power being black.

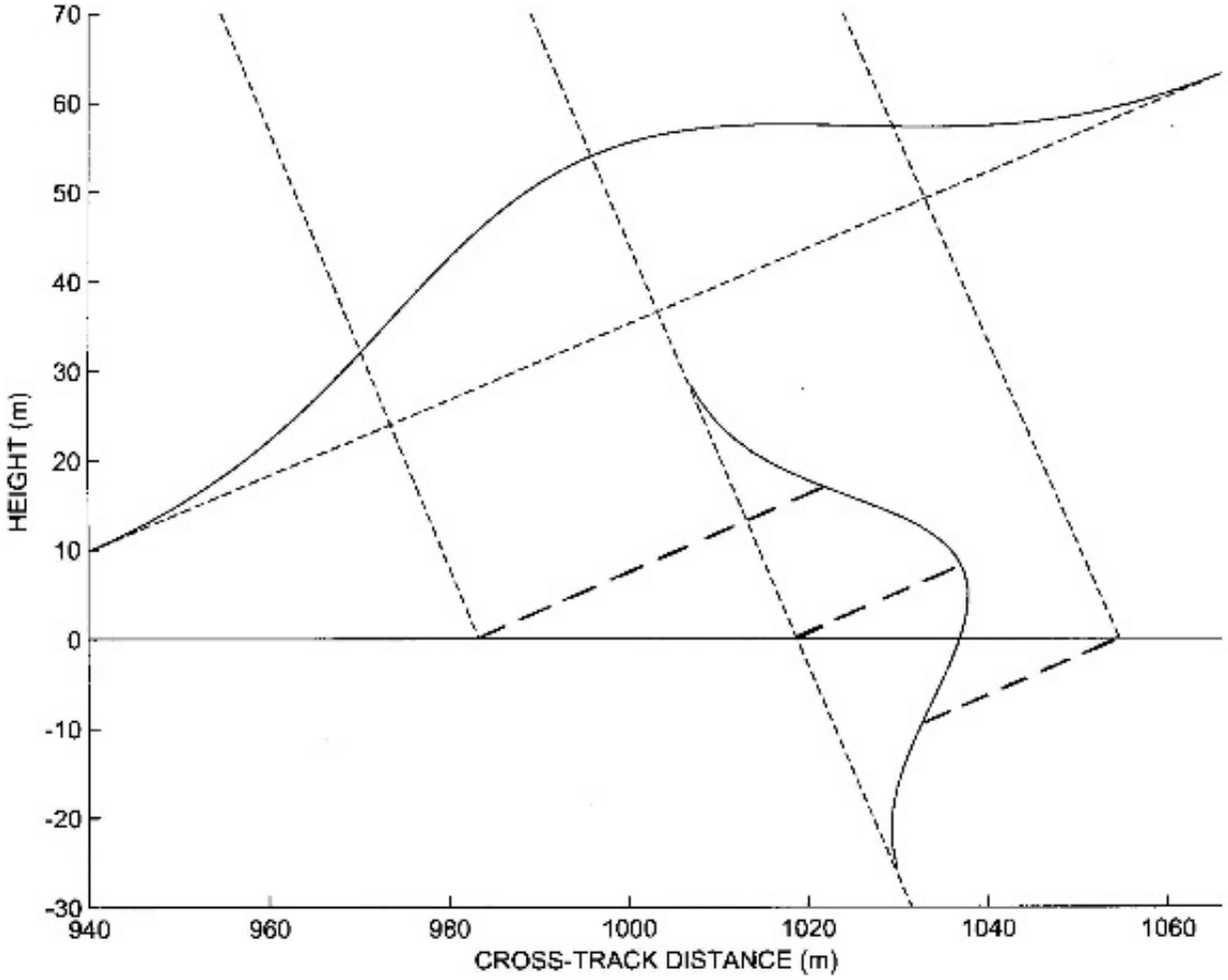

FIG. 3. WSRA narrow beam, represented by a Gaussian gain variation, boresighted on a flat sea surface from 2400 m at a 23º off-nadir incidence angle.

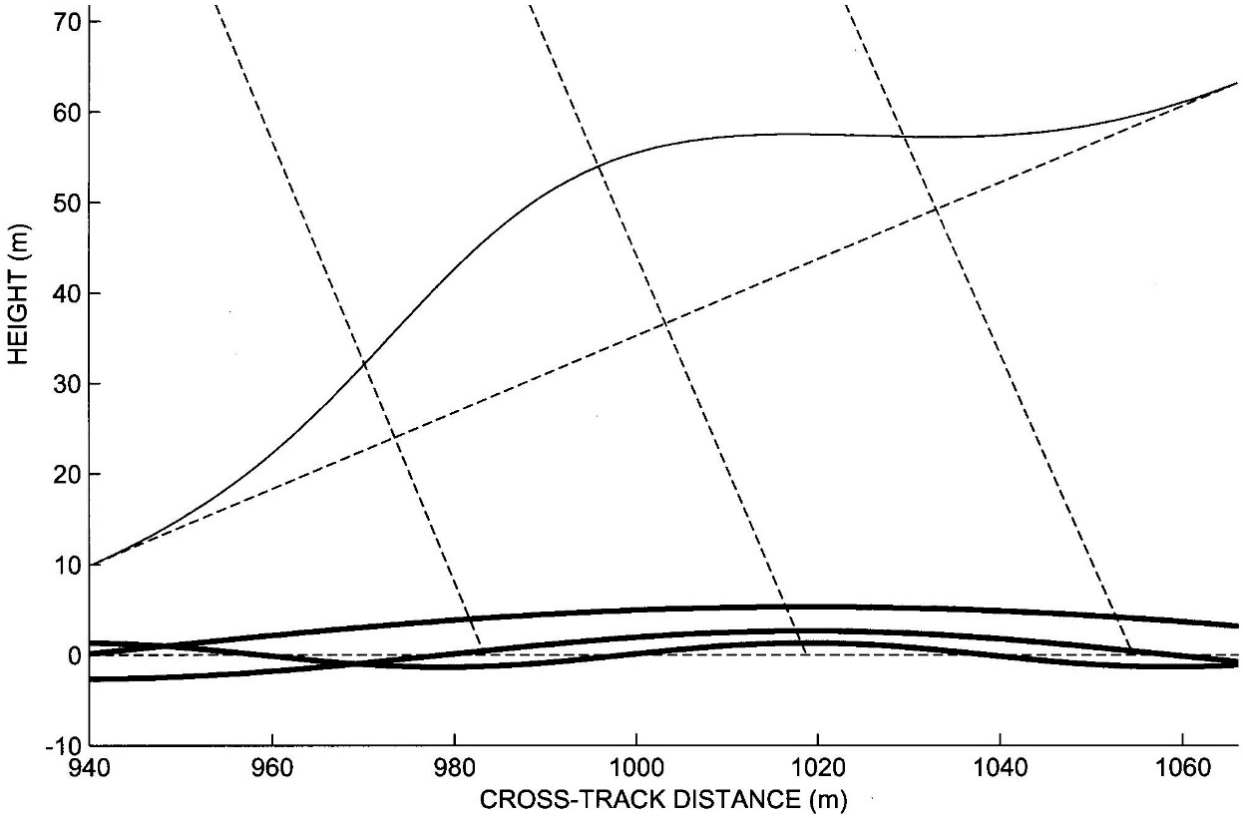

FIG. 4. WSRA narrow beam of Figure 3 boresighted at the crest of ocean waves of 80, 160 and 320 m wavelength with wavelength to wave height ratios of 30.

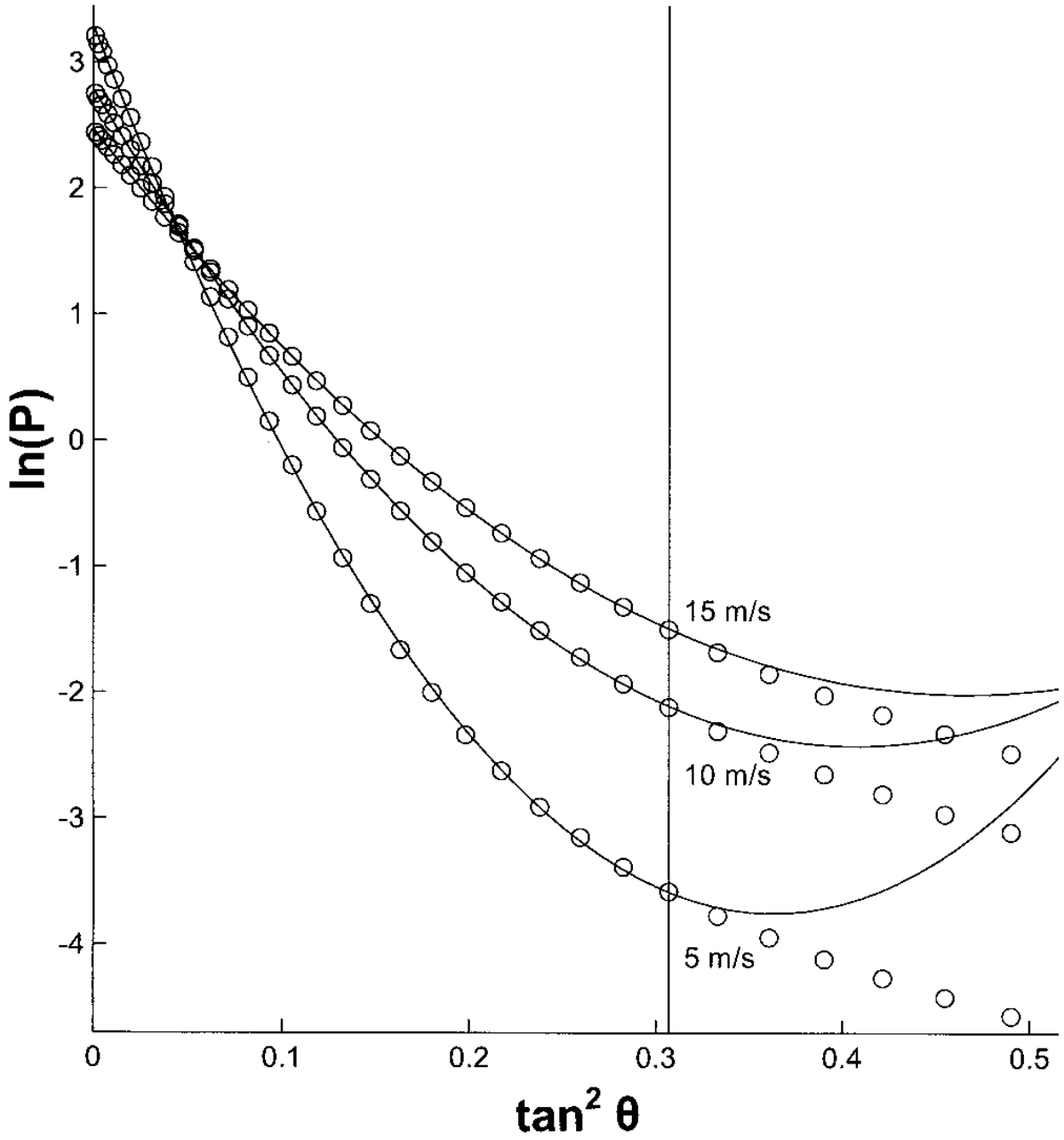

FIG. 5. Voronovich and Zavorotny (2001) 14 GHz theoretical backscattered power variation with incidence angle (circles) and fitted quadratic curves (1). This is Figure 3 of Walsh et al. (2008).

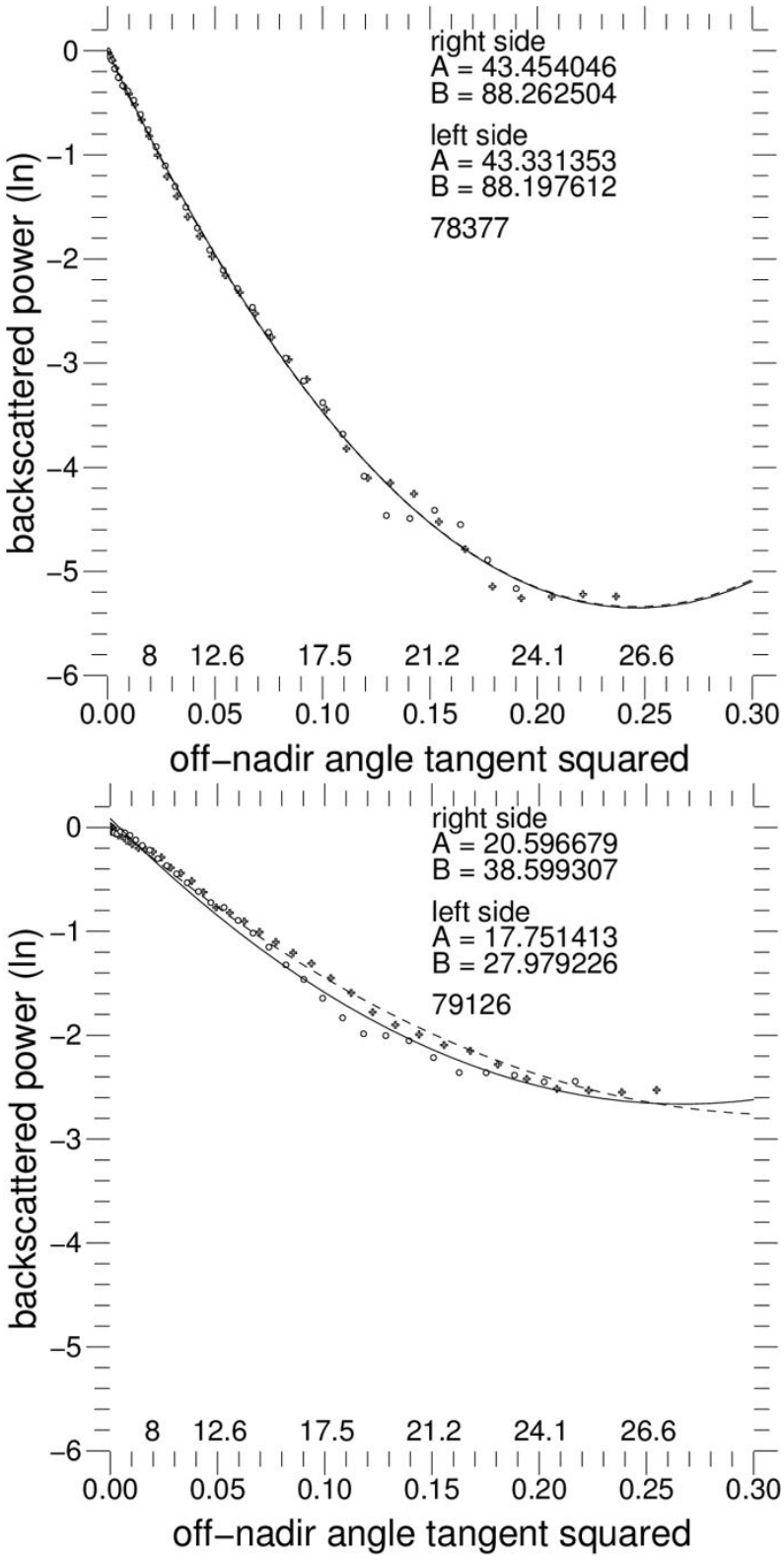

FIG. 6. Variation of backscattered power with off-nadir incidence angle averaged over 500-line segments of WSRA data.

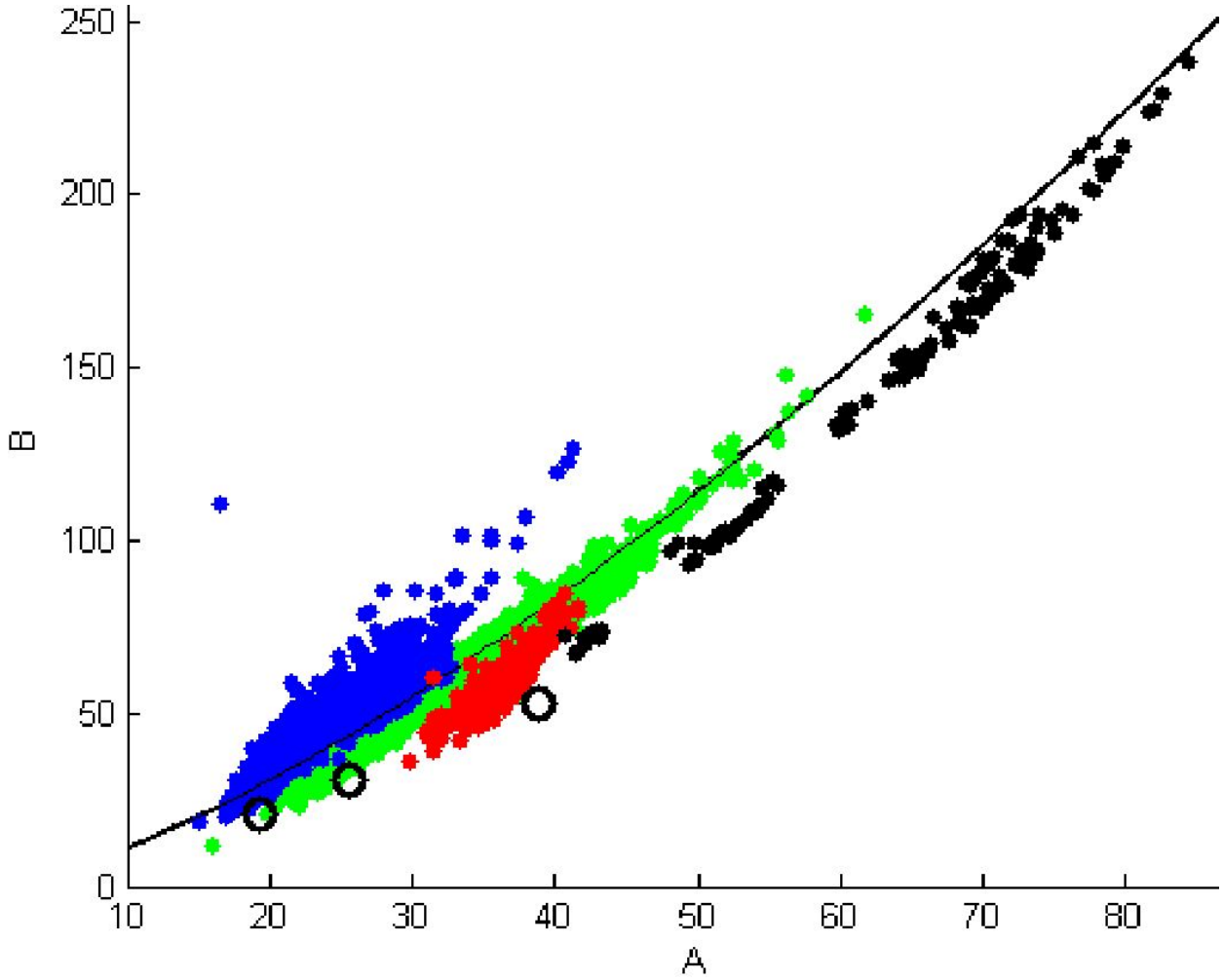

FIG. 7. *B* vs *A* values determined from WSRA 16 GHz data for four flights: (1) Hurricane Irene in the Atlantic Ocean on 25 August 2011 (blue), (2) Tropical Storm Karen in the Gulf of Mexico on 3 October 2013 (green), (3) Calwater 2015 in the Pacific Ocean on 9 February 2015 (red), and (4) a low wind test flight in the Gulf of Mexico in 2015 (black). The three open circles are from the Voronovich and Zavorotny (2001) theoretical computation at 14 GHz.

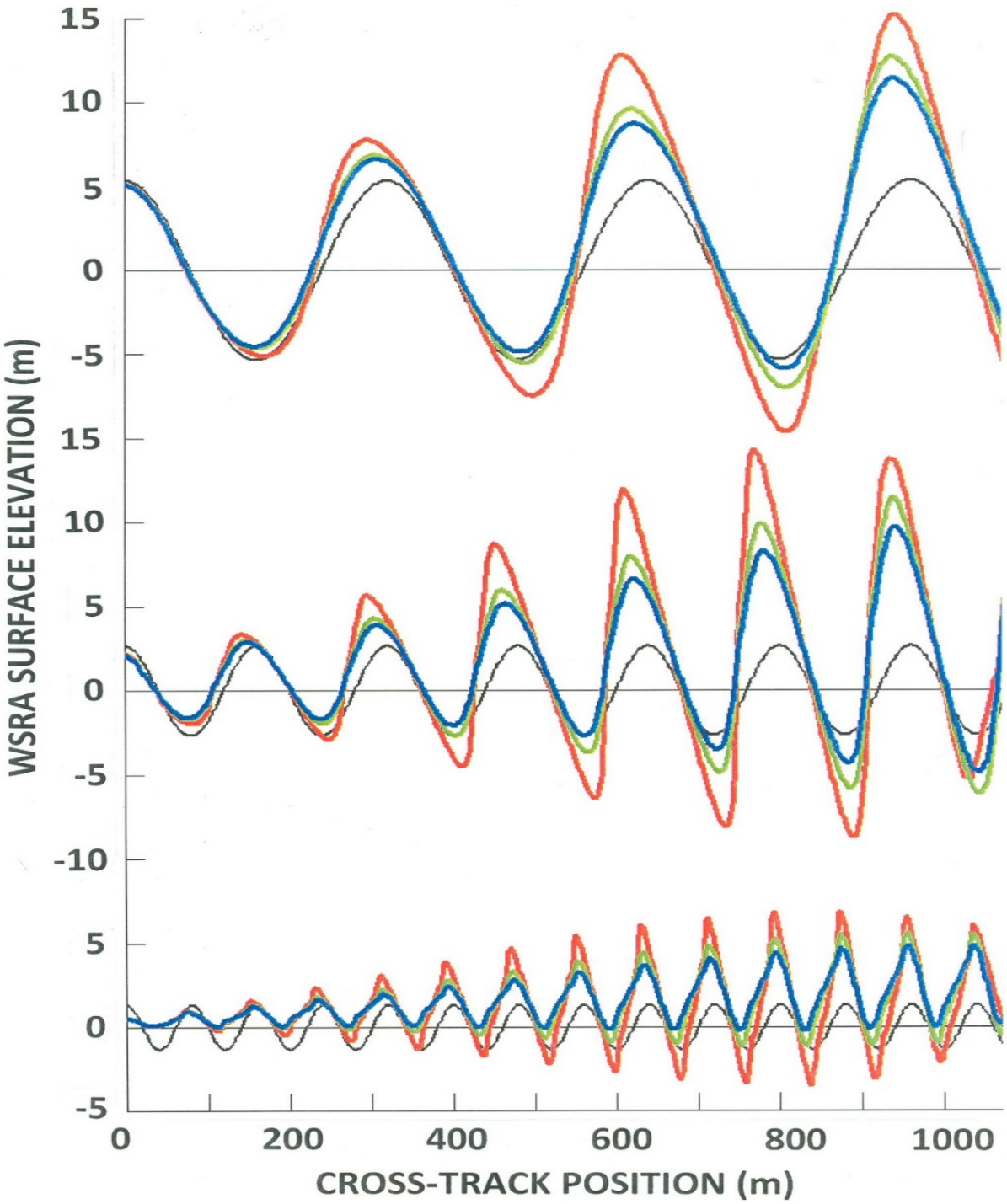

FIG. 8. Simulated WSRA-observed wave profiles generated for an aircraft altitude of 2.5 km and long-crested sinusoidal waves propagating across the swath with wavelengths of 320 m (top), 160 m (middle) and 80 m (bottom) and mss values of 0.08 (blue), 0.05 (green) and 0.02 (red). Black curves indicate the actual wave profiles with wavelength to wave height ratio of 30.

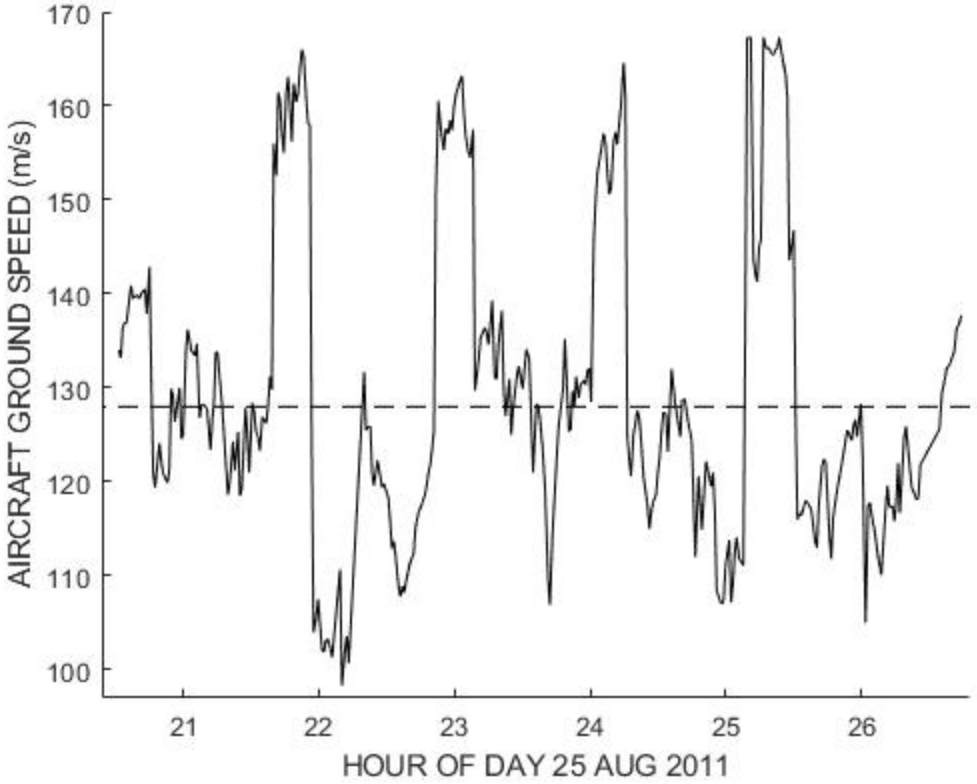

FIG. 9. Ground speed variation during the flight into Hurricane Irene on 25 August 2011.

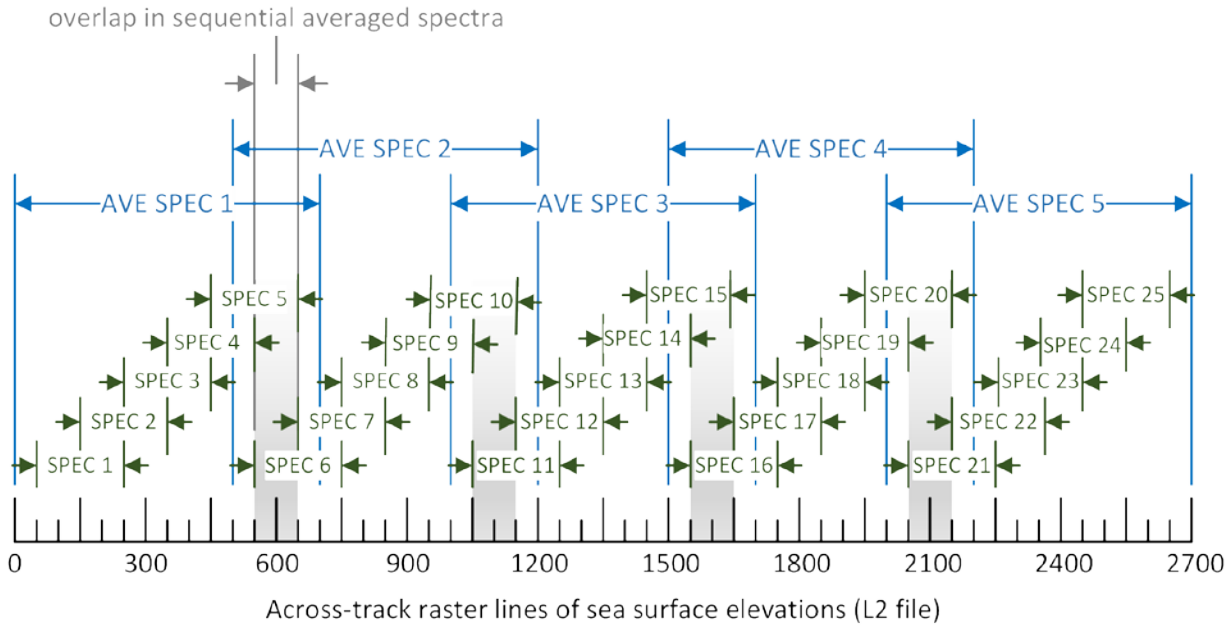

FIG. 10. The WSRA data processing timing diagram for calculating L3 output spectra for a ground speed of 128 m/s. The individual spectra (in green) contain 200 raster lines at a ground speed of 128 m/s, and 150 and 300 raster lines at ground speeds of 170 and 85 m/s.

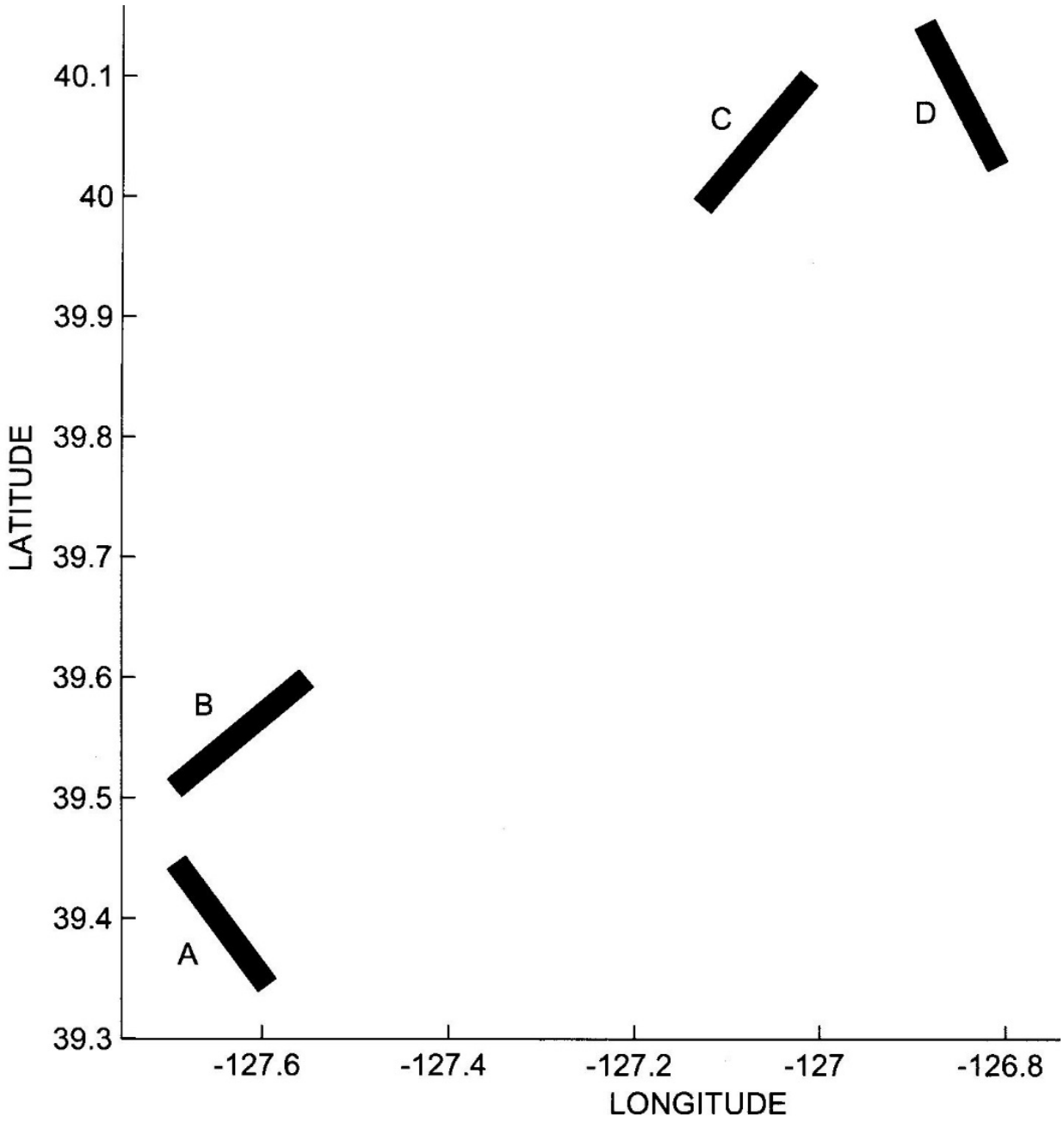

FIG. 11. Four areas of interest during the CalWater 2015 experiment flight on 9 February 2015. Each area contained 1300 raster lines of WSRA topography.

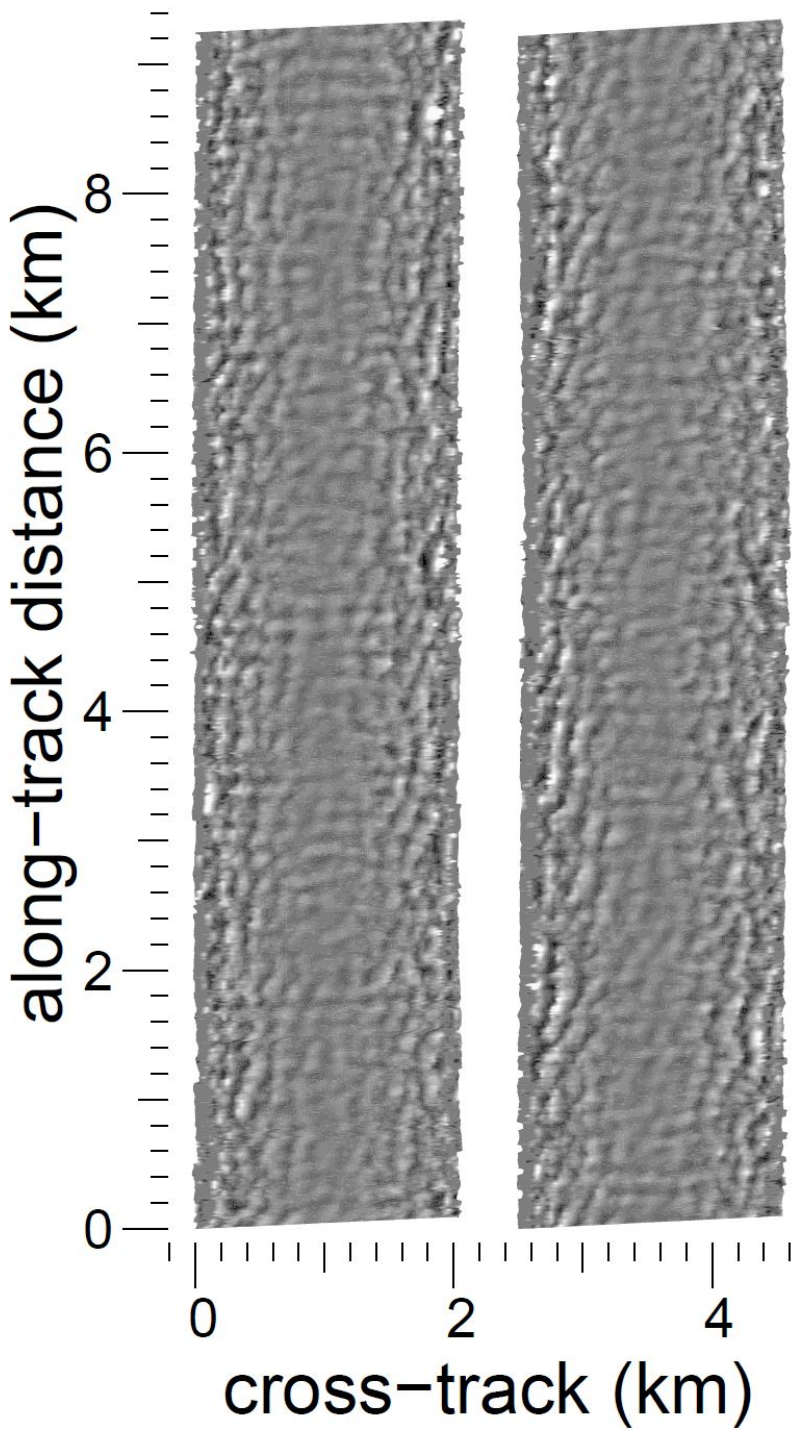

FIG. 12. Wave topography generated from 1700 consecutive raster lines of WSRA data acquired while the aircraft was flying northwest, displayed with a ±9 m grayscale. The first 850 raster lines are in the right image, bottom to top, and the next 850 lines are in the left image.

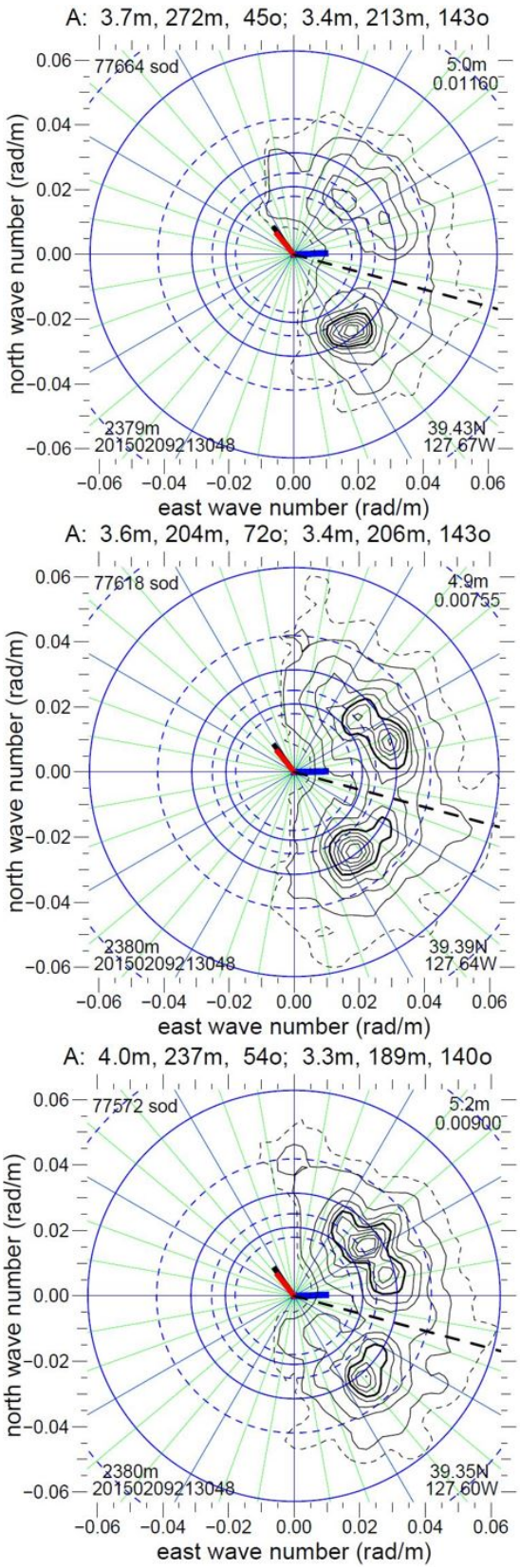

FIG. 13. L4 directional wave spectra generated from Figure 12 wave topography.

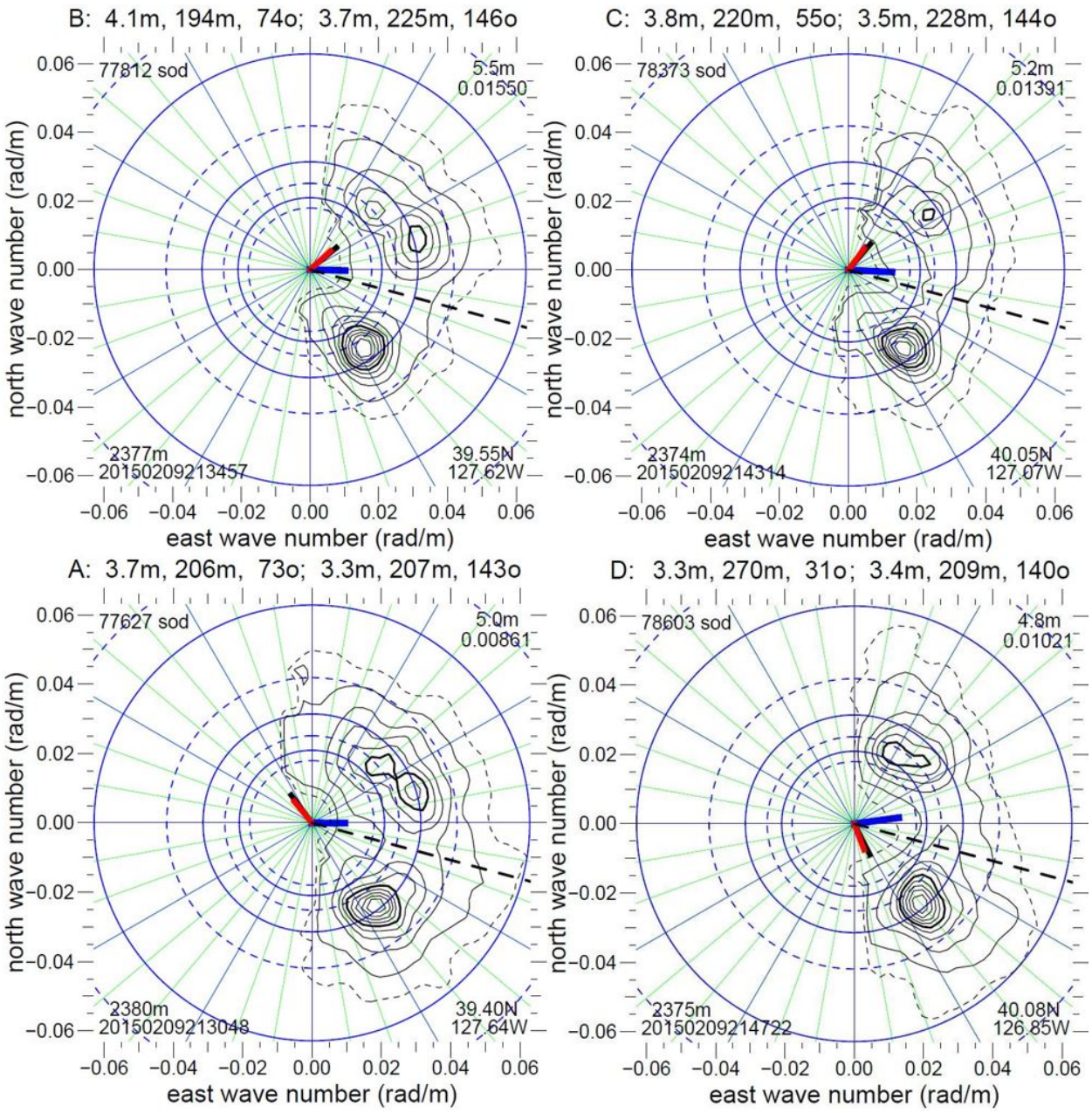

FIG. 14. Wave spectra generated from sets of 1300 raster lines of WSRA wave topography contained in the areas indicated in Figure 11. The spectrum annotations are the same as Figure 13.

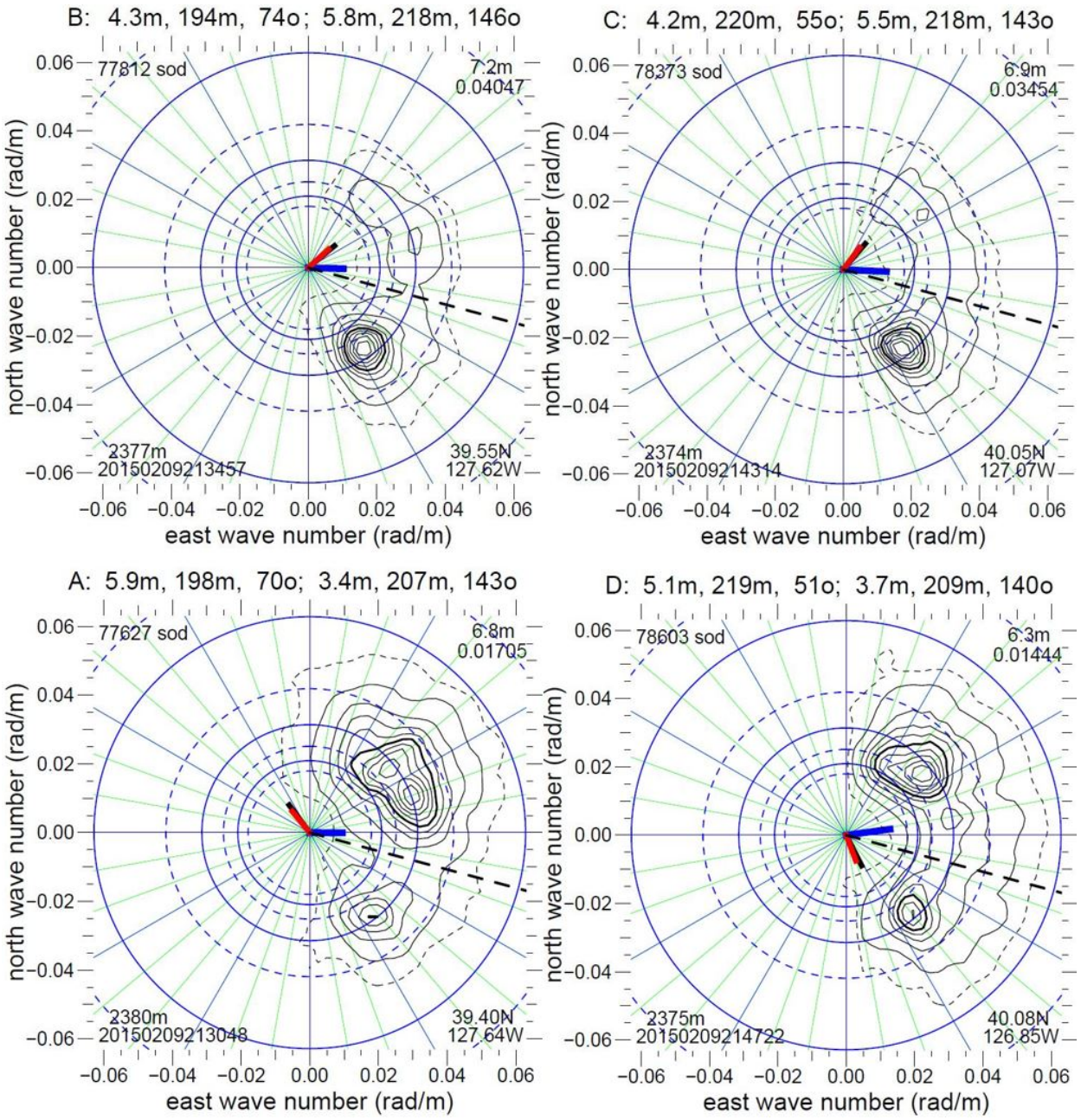

FIG. 15. The same wave spectra of Figure 14, but before variance correction.

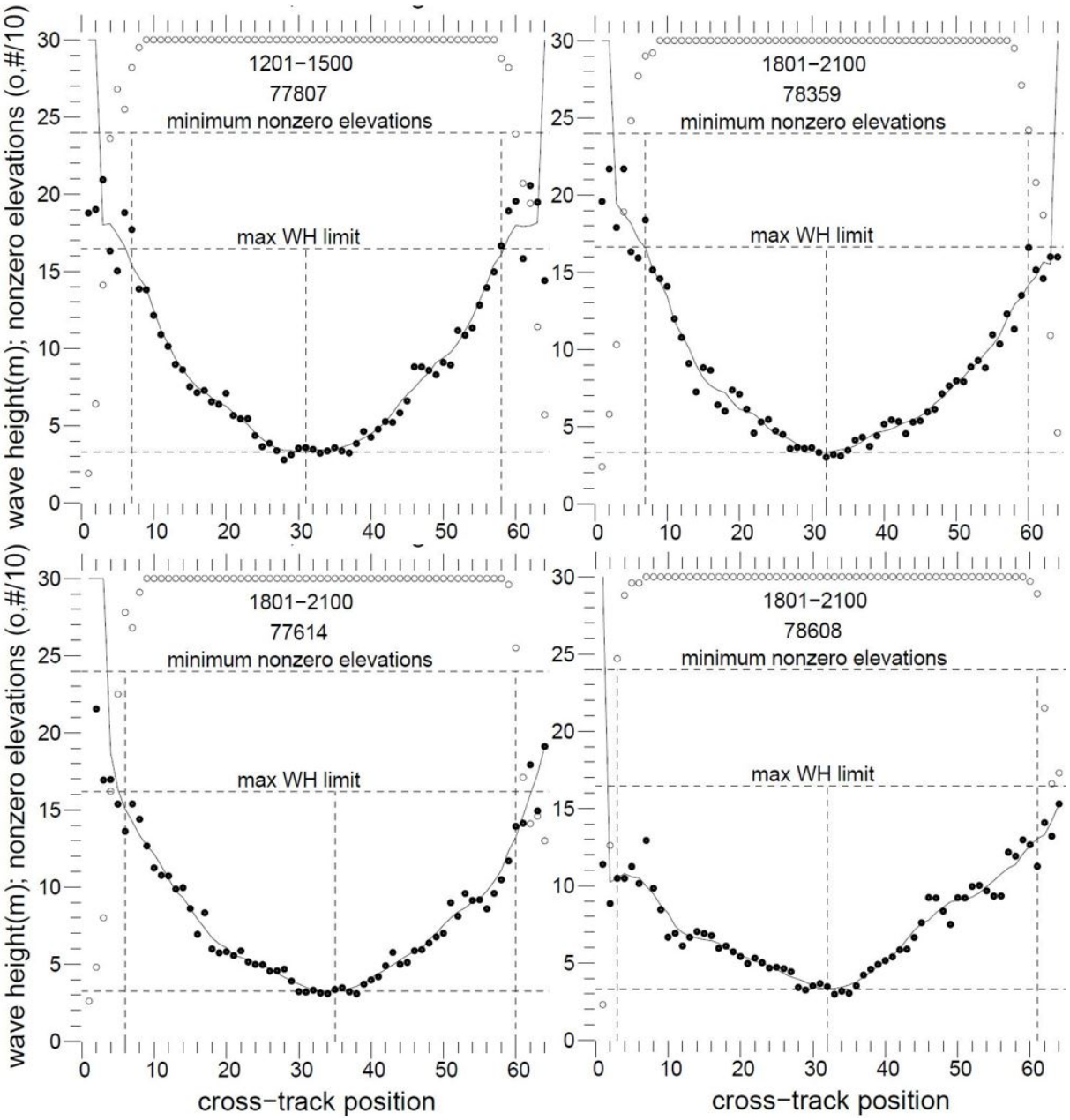

FIG. 16. Cross-track variation of the apparent wave height (filled circles) at locations A, B, C and D in Figure 11, computed as four times the standard deviation of the elevations at each of the 64 cross-track positions of the wave topography, computed from segments of 300 consecutive raster lines. Open circles indicate the number of valid elevations at each cross-track position. The relative positions of the four data sets within this figure are the same as in Figures 14 and 15. The 5-digit numbers are seconds of the day.

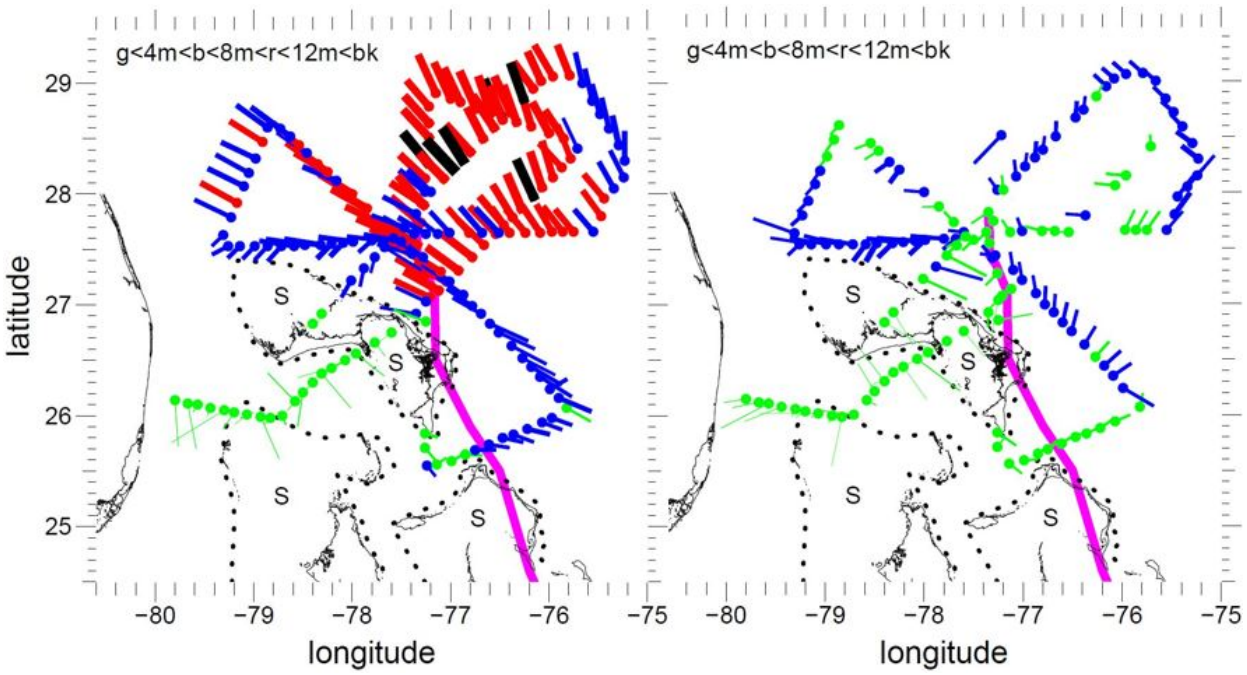

FIG. 17. Geographic coordinate vector maps of the WSRA primary (left) and secondary (right) wave fields during the Hurricane Irene flight on 25 August 2011. The magenta curve shows the track of Irene. Four areas of shallow water (<10 m depth) in the vicinity of the islands are indicated by S enclosed by dots. The colored dots indicate some of the locations of WSRA directional wave spectra. Radials extend from them in the wave propagation direction a length proportional to wavelength. Radial widths are proportional to wave height and are color-coded in four wave height intervals indicated at the top of the plots.

.

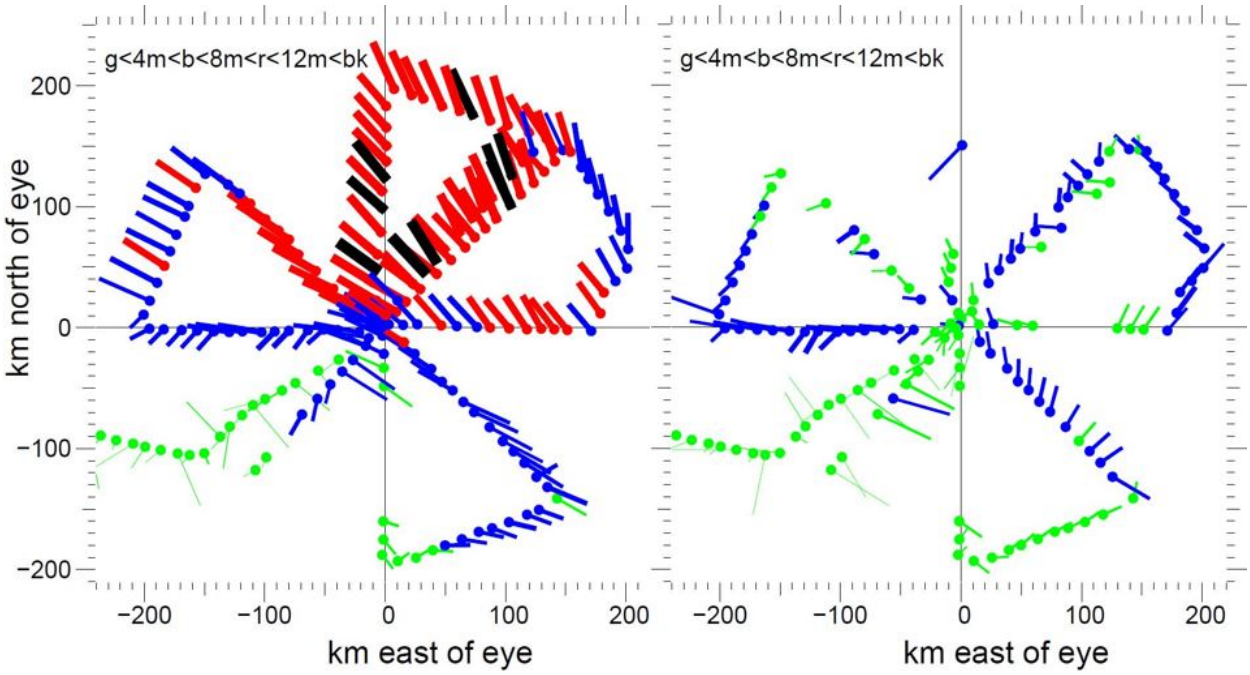

FIG. 18. Hurricane Irene storm-relative wave vector maps using the same format as Figure 17.

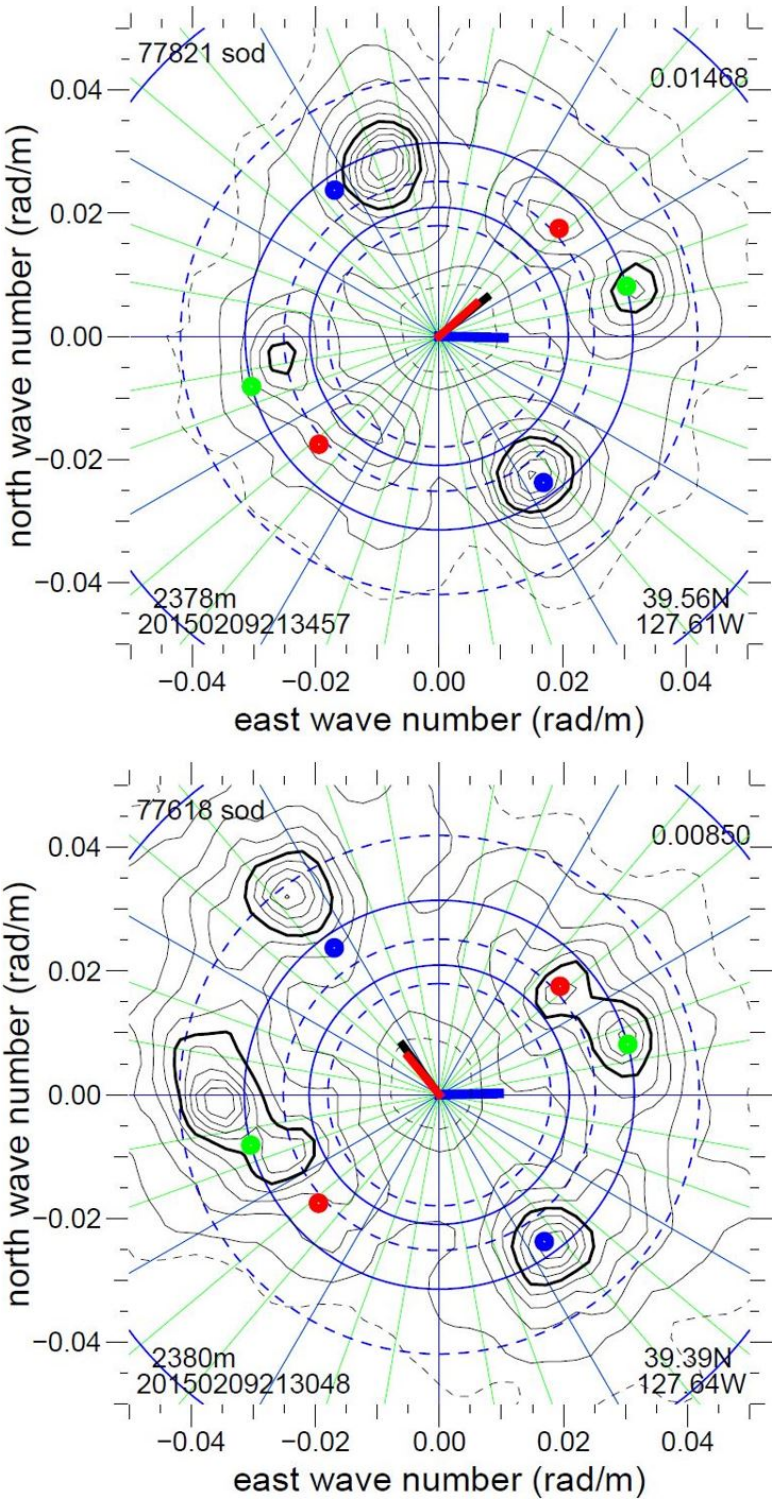

FIG. A1. WSRA directional wave spectra from the Calwater 2015 flight on 9 February 2015 that have been Doppler- and variance-corrected without deleting the artifact lobes. The colored dots are perfectly symmetrical reference points in identical positions in the two spectra.

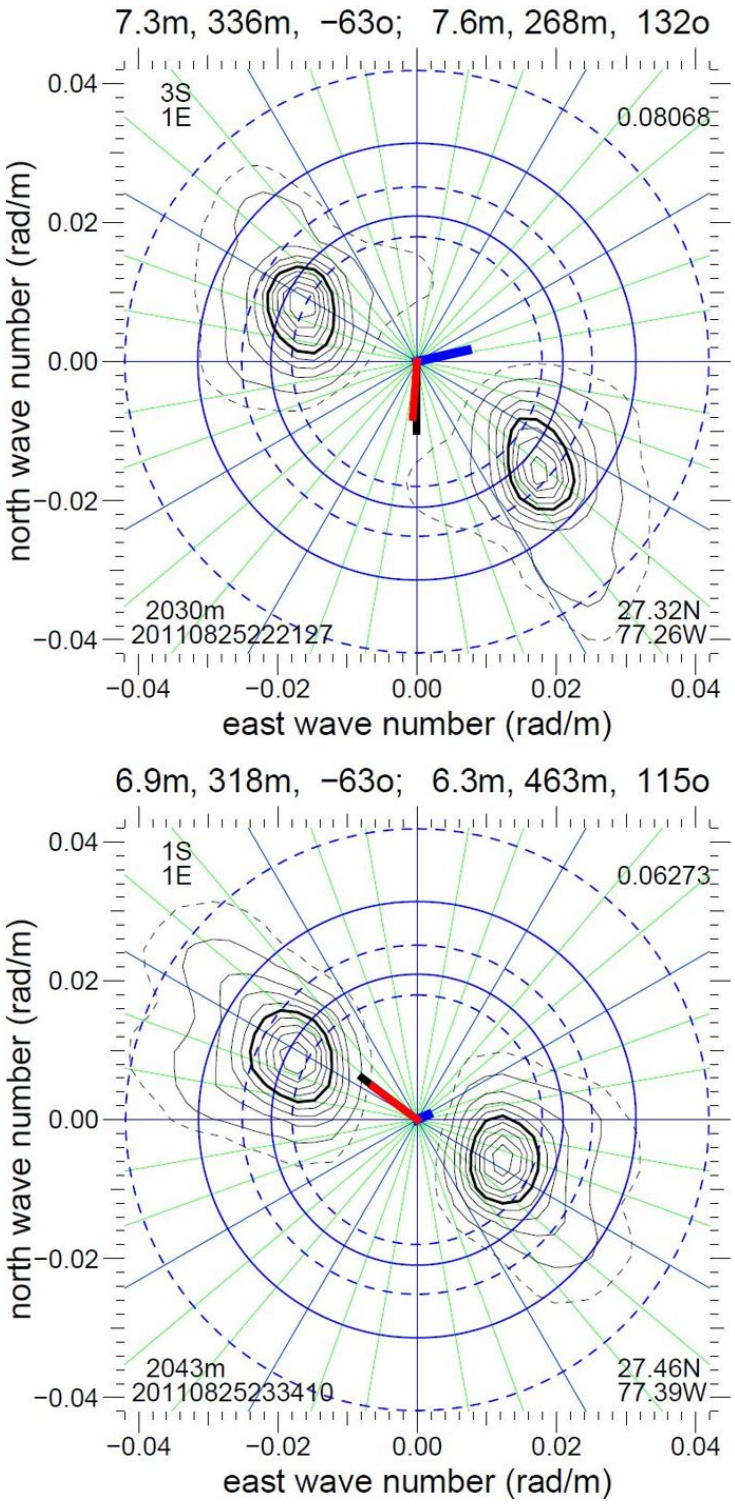

FIG. A2. WSRA directional wave spectra from Hurricane Irene that have been Doppler- and variance-corrected without deleting the artifact lobes. Upper left corner numbers are km displacements from the eye.

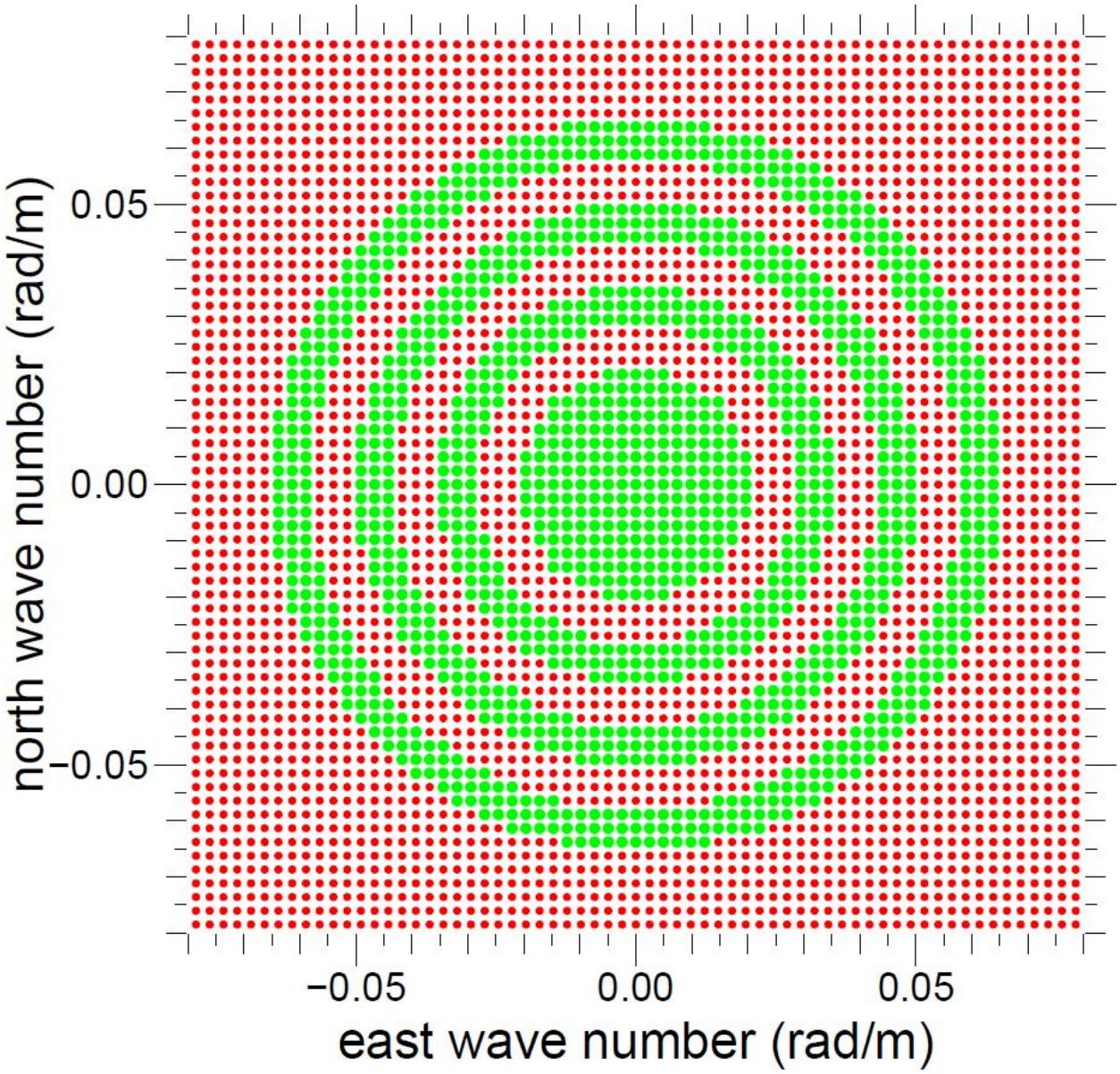

FIG. A3. WSRA directional wave spectrum points with alternating red and green colors identifying the eight spectral regions that wind-forcing predicted wave propagation directions are applied to.

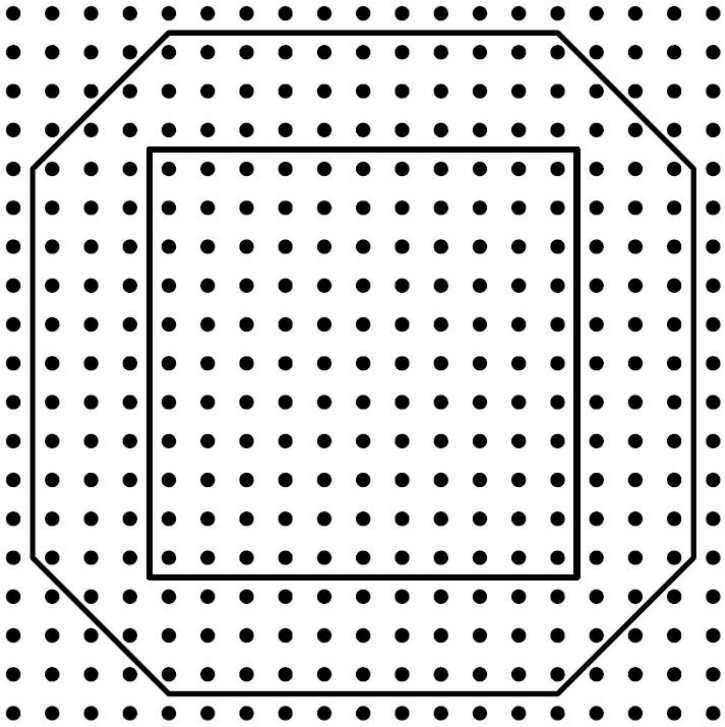

FIG. A4. Regions surrounding an L3 real spectral maximum that are transferred to the output spectrum automatically (square) and potentially (octagon) if the variance continues to decrease.